Advances in Colloid and Interface Science 236 (2016) 63–82

Contents lists available at ScienceDirect

Advances in Colloid and Interface Science

journal homepage: www.elsevier.com/locate/cis

Droplet dynamics in rotating flows

B. Maneshian [a,b], Kh. Javadi [b], M. Taeibi Rahni [a], R. Miller [c]

[a] Aerospace Research Institute (Ministry of Science, Research and Technology), Tehran, Iran
[b] Aerospace Department, Sharif University of Technology, Azadi Ave., Tehran, Iran
[c] Max Planck Institute of Colloids and Interfaces, Potsdam-Golm Science Park Am Mühlenberg 1 OT Golm 14476 Potsdam Denmark

ARTICLE INFO

Available online 29 July 2016

Keywords:
Two-phase flow
Droplet dynamics
Rotating flow
Lattice Boltzmann Method

ABSTRACT

This paper deals with investigations of droplet dynamics in rotating flows. In many previous studies droplet dynamics was analyzed in simple unidirectional flows. To fill this gap, the focus of this study is an overview on investigations of droplet dynamics in a complex rotating flow. A Lattice Boltzmann Method with high potential in simulation of two-phase unsteady flows is applied to simulate the physics of the problem in a lid-driven cavity. In spite of its simple geometry, there is a complex rotating flow field containing different vortices and shear regions. The Reynolds number based on the cavity length scale and the upper wall velocity, Re_L, is considered to be 1000. We discuss here effects of different parameters such as: density ratios (1, 5, 10, 100, and 1000), droplet sizes (D/L = 0.097, 0.114, 0.131 and 0.2), and droplet initial positions (1/8, 2/8, and 3/8 of the cavity length, L, out of center). The results are discussed in terms of global flow physics and its interaction with the droplet, drop deformation during its motion along with the main flow, and droplet trajectories. It is shown that there are strong interactions between the droplet and the main carrying flow. During motion, the droplets pass through different flow regions containing acceleration/deceleration zones. Consequently, the droplets experience different shear forces resulting in stretching, shrinking, rotating and dilatation which all contribute to the dynamics of the droplet.

1. Introduction

Investigation of droplet and bubble dynamics is one of the challenging phenomena in many science and engineering problems such as emulsification processes, food industry, polymer blending and oil recovery, and in deformation of biological cells [1]. In these processes, two immiscible fluids are mixed to obtain a distribution of droplets of one liquid in the other. So, many investigations have been done including experimental, numerical, and theoretical studies.

Numerous research activities have focused on the relationship between flow and drop deformation since the seminal work of Taylor [2,3] which includes both theoretical analysis and experimental observations focused on the deformation of single droplets suspended in a second liquid to which either a simple shear or planar elongation flow was applied. Some major improvements of Taylor's theoretical work go back to Chaffey and Brenner [4], Cox [5] and Barthès-Biesel and Acrivos [6]. However, in order to treat the situation in which drops are highly extended, the theory initially developed by Taylor [7] has been applied by e.g. Buckmaster [8,9], Acrivos and Lo [10], Rallison and Acrivos [11], Hinch and Acrivos [12,13], Yu et al. [14] and Dressler and Edwards [15].

Also, many analytical models have been applied to predict the droplet breakup or its deformation in a given flow field. In this case, direct numerical simulations have been employed in a number of studies which were based either on the volume of fluid (VOF) method, Li et al. [16], Renardy et al. [17] and Renardy and Renardy [18] or on the boundary integral method (BIM), [19–25]. Many experimental contributions were performed as well [26–40]. These include measurements of the critical capillary number over a wide range of both simple shear and planar elongation and computer controlled versions of Taylor's four roll mill and shear band apparatus.

Among the numerical studies, some researchers applied the Lattice Boltzmann Method (LBM) to simulate the dynamics, deformation and breakup of droplet. Inamuro et al. [41], Sman and Graaf [42] and Farokhirad et al. [43] are examples of those droplet dynamics studies by LBM.

Droplet dynamics, its deformation and breakup are complex phenomena. This complexity becomes more complicated when the droplet is considered in a rotating flow. To the best of our knowledge, information about droplet dynamics in rotating flows is very scarce. However, some researchers tried to study this problem, but none of them made detailed investigations on the corresponding physics. For example, Xin and Megaridis [44] studied the fluid dynamics between a linear periodic array of droplets and a concentric cylinder in a rotating tube configuration. Egholm et al. [45] investigated the

E-mail addresses: maneshian@gmail.com (B. Maneshian), kjavadi@sharif.edu (K. Javadi), taeibi@sharif.edu (M.T. Rahni), Reinhard.Miller@mpikg.mpg.de (R. Miller).

http://dx.doi.org/10.1016/j.cis.2016.07.005
0001-8686/

droplet trajectories and the droplet deformations in a rotor-stator device consisting of two concentric cylinders with teethed walls. Poon et al. [46] studied a uniform flow passing on a rotating droplet in a rectangular channel and Arkhipov et al. [47] investigated the effect of angular velocity and the droplet size on the trajectories of a droplet (as a solid body) in a rotating flow. Also, some studies have been carried out to investigate droplet dynamics in Taylor–Couette devices [48–56].

The focus of this work is to study the complex phenomenon of droplet dynamics in a rotating flow more deeply. Droplet deformations, such as stretching, shrinkage, breakup and droplet pathline and its interaction with the rotating flow are discussed here. Also, effects of the density ratio, droplet diameter and the initial position of the droplet are studied. In order to simulate the problem, the LBM is applied. Compared with other two-phase LBMs based on [57,58] and [59] the present approach [60,61] is capable of eliminating parasitic currents and handling higher density ratios. Note, in contrast to a solid rotating body the droplet dynamics is studied here in a rotating flow within a cavity in which the flow has different vortices.

2. Problem description and numerical method

This section deals with the description of the geometrical configuration of the problem and the numerical Lattice Boltzmann Method applied to simulate the physics.

2.1. Problem description

The schematic of the configuration analyzed in this study is illustrated in Fig. 1. A circular droplet is considered in a cavity with the aspect ratio one in which the upper wall has the velocity U while the other walls are fixed. The Reynolds number based on the cavity length scale and the upper wall velocity, Re_L, is considered to be 1000. Also, the Reynolds number based on the droplet diameter is, $Re_D = 130$ and the capillary number equals, $Ca = 0.8$, which is defined as $Ca = \frac{U\mu}{\sigma}$. The problem is solved numerically for different density ratios, different droplet sizes and various initial positions of the droplet.

2.2. Numerical method

This subsection deals with the numerical procedure and the application of the physical boundary conditions in the numerical procedure.

2.2.1. Numerical procedure

The Lattice Boltzmann Method (LBM) is a modern approach in Computational Fluid Dynamics (CFD). It is often used to solve the incompressible, time-dependent Navier–Stokes equations numerically. Its strength lies however in the ability to easily represent complex physical phenomena, ranging from multiphase flows to chemical interactions between the fluid and the surroundings. The method finds its origin in a molecular description of a fluid and can directly incorporate physical terms stemming from knowledge of the interaction between molecules. It has proven to be an efficient and convenient alternative to traditional solvers for a large variety of industrial problems. Typical achievements of a LBM are parallel data analysis, post-processing and evaluation, fully resolved multi-phase flow with small droplets and bubbles, fully resolved flow through complex geometries and porous media and complex, coupled flow with heat transfer and chemical reactions.

The LBM uses only local data communication to update a particle distribution function $f_\alpha(x,t)$ at each time step. In the LBM, particle density distribution functions $f_\alpha(x,t)$ at point x and time t are confined to move synchronously on a regular lattice, where α denotes the direction of the lattice link. The distribution functions interact on the lattice in a way to conserve mass, momentum, isotropy, and Galilean invariance. Here, we assume a two-dimensional and nine-velocity (D2Q9) lattice for simulation which is illustrated in Fig. 2.

In terms of the distribution function, the general discrete Boltzmann equation [62] is:

$$f_\alpha(x + e_\alpha \Delta t, t + \Delta t) = f_\alpha(x,t) + \Omega_\alpha(x,t), \tag{1}$$

where, e_α represents discrete lattice velocities in the direction of link α. In addition,

$$e_\alpha = (0,0) \qquad \alpha = 0, \tag{2}$$

$$e_\alpha = \left[\cos\left(\frac{\pi}{2}(\alpha-1)\right), \sin\left(\frac{\pi}{2}(\alpha-1)\right)\right], \qquad \alpha = 1,2,3,4 \tag{3}$$

$$e_\alpha = \sqrt{2}\left[\cos\left(\frac{\pi}{2}(\alpha-1)+\frac{\pi}{4}\right), \sin\left(\frac{\pi}{2}(\alpha-1)+\frac{\pi}{4}\right)\right], \qquad \alpha = 5,6,7,8 \tag{4}$$

and $f_\alpha(x,t)$ is the particle density distribution function and $\Omega_\alpha(x,t)$ is the collision operator [62,63] as:

$$\Omega_\alpha(x,t) = -\frac{1}{\lambda}\left[f_\alpha(x,t) - f_\alpha^{eq}(x,t)\right], \tag{5}$$

in which, λ is the relaxation time.

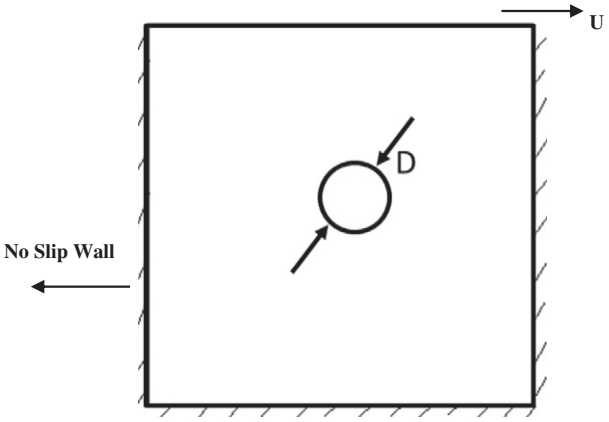

Fig. 1. Geometrical configuration of the problem.

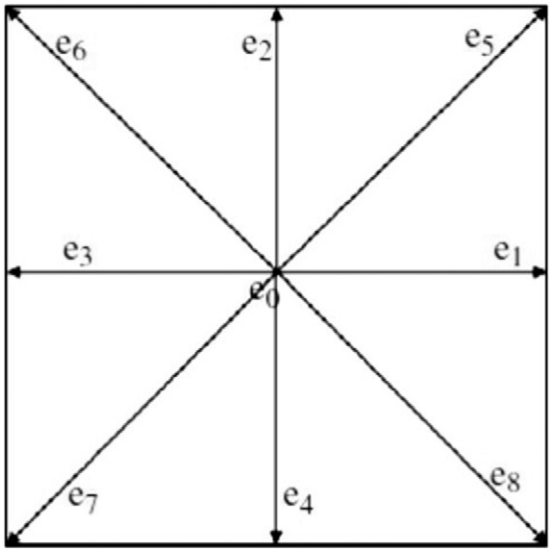

Fig. 2. The two-dimensional and nine velocity D2Q9 model.

Two particle distribution functions, g_α and h_α are applied in the present LBM for binary fluids [61]. The function h_α is used as a phase-field function for the transport of the composition C of one component, and the function g_α is used for the calculation of pressure and momentum of the two-component mixture. The discrete Boltzmann equations for the phase-field advection equation and the pressure evolution and momentum equations are, respectively:

$$\frac{\partial h_\alpha}{\partial t} + \boldsymbol{e}_\alpha \cdot \nabla h_\alpha = -\frac{h_\alpha - h_\alpha^{eq}}{\lambda} + (\boldsymbol{e}_\alpha - \boldsymbol{u}) \cdot \left[\nabla C - \frac{C}{\rho c_s^2}(\nabla p - \mu \nabla C)\right] \Gamma_\alpha + \nabla \cdot (M \nabla \mu) \Gamma_\alpha, \tag{6}$$

$$\frac{\partial g_\alpha}{\partial t} + \boldsymbol{e}_\alpha \cdot \nabla g_\alpha = -\frac{g_\alpha - g_\alpha^{eq}}{\lambda} + (\boldsymbol{e}_\alpha - \boldsymbol{u}) \cdot \left[\nabla \rho c_s^2 (\Gamma_\alpha - \Gamma_\alpha(0)) + \mu \nabla C\right], \tag{7}$$

where the equilibrium distribution functions are given as:

$$h_\alpha^{eq} = t_\alpha C \left[1 + \frac{\boldsymbol{e}_\alpha \cdot \boldsymbol{u}}{c_s^2} + \frac{(\boldsymbol{e}_\alpha \cdot \boldsymbol{u})^2}{2c_s^4} - \frac{\boldsymbol{u} \cdot \boldsymbol{u}}{2c_s^2}\right], \tag{8}$$

$$g_\alpha^{eq} = t_\alpha \left[p + \rho c_s^2 \left(\frac{\boldsymbol{e}_\alpha \cdot \boldsymbol{u}}{c_s^2} + \frac{(\boldsymbol{e}_\alpha \cdot \boldsymbol{u})^2}{2c_s^4} - \frac{\boldsymbol{u} \cdot \boldsymbol{u}}{2c_s^2}\right)\right]. \tag{9}$$

In these equations, $\boldsymbol{u}$ represents volume averaged velocity, c_s is the basic speed on the lattice, ρ is the mixture density, μ is the chemical potential and M is the mobility in the Cahn–Hilliard diffusion. Also, Γ_α is defined as:

$$\Gamma_\alpha = t_\alpha \left[1 + \frac{\boldsymbol{e_\alpha} \cdot \boldsymbol{u}}{\boldsymbol{c_s^2}} + \frac{(\boldsymbol{e_\alpha} \cdot \boldsymbol{u})^2}{2\boldsymbol{c_s^4}} - \frac{(\boldsymbol{u} \cdot \boldsymbol{u})}{2c_s^2}\right]. \tag{10}$$

The composition, momentum and dynamic pressure can be obtained by taking the moments of h_α and g_α:

$$C = \sum_\alpha h_\alpha, \tag{11a}$$

$$\rho \boldsymbol{u} = \frac{1}{c_s^2} \sum_\alpha \boldsymbol{e}_\alpha g_\alpha, \tag{11b}$$

$$p = \sum_\alpha g_\alpha. \tag{11c}$$

For detailed discretization of Eqs. (6) and (7), we want to refer to Lee and Liu [61].

The mixture density ρ can be measured as $\rho = \rho_h C + \rho_l (1\text{-}C)$, in which ρ_h and ρ_l are the bulk densities of the two fluids. The mixing energy density for binary fluids can be calculated as $E_0(C, \nabla C) = E_0(C) + \kappa |\nabla C|^2/2$, where κ is the gradient parameter and $E_0(C) = \beta C^2 (1\text{-}C)^2$ is the bulk energy density with constant β [61]. The equilibrium profile is obtained by minimizing the mixing energy. The equilibrium interface profile is then $C(z) = 1/2 + \tanh(2z/D)/2$, where z is the coordinate normal to the plane interface and D is the numerical interface thickness. Having D and the interfacial tension σ, the values of β and κ can be determined as $\beta = 12\sigma/D$ and $\kappa = \beta D^2/8$.

2.2.2. Boundary conditions

The performance of the LBM boundary conditions is simple compared to conventional CFD techniques. To perform boundary conditions, we have to calculate suitable unknown distribution functions from known distribution functions. Fig. 3 illustrates the known (solid lines) and unknown (dotted lines) particle density distribution functions on all walls of the cavity. We performed the standard bounceback boundary conditions [64] on all fixed solid walls to calculate the unknown particle distribution functions. In applying a standard bounceback boundary conditions for our physical boundary conditions,

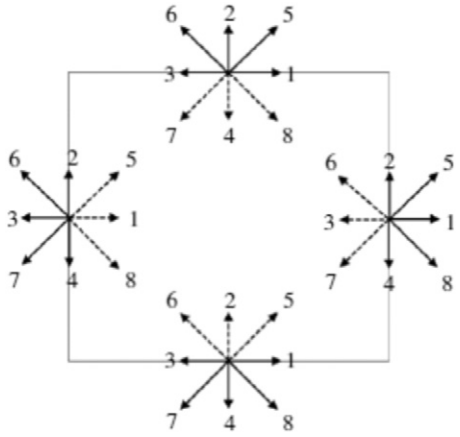

Fig. 3. Known and unknown particle density distributions for the boundaries of the cavity.

the general particle density distribution functions, f_α, on the left wall of the cavity are:

$$f_1 = f_3, \quad f_5 = f_7, \quad f_8 = f_6. \tag{12}$$

The particle distribution functions on the right wall of the cavity are:

$$f_3 = f_1, \quad f_6 = f_8, \quad f_7 = f_5. \tag{13}$$

The particle distribution functions on the bottom wall of the cavity are

$$f_2 = f_4, \quad f_5 = f_7, \quad f_6 = f_8. \tag{14}$$

On the moving wall, the equilibrium distribution functions are used to compute the unknown particle distribution functions. The particle density distribution functions on the moving wall are:

$$f_4 = \frac{1}{9}\rho\left[1 - 3v + \frac{9}{2}v^2 - \frac{3}{2}(u^2 + v^2)\right], \tag{15}$$

$$f_7 = \frac{1}{36}\rho\left[1 + 3(-u - v) + \frac{9}{2}(u + v)^2 - \frac{3}{2}(u^2 + v^2)\right], \tag{16}$$

$$f_8 = \frac{1}{36}\rho[1 + 3(u - v) + \frac{9}{2}\left(u - v\right)^2 - \frac{3}{2}(u^2 + v^2)\right]. \tag{17}$$

3. Validation of results

This section contains validation and verification of the results presented in five following subsections. In the first part, the current numerical results are compared with analytical ones for demonstrating that the simulation of a two-phase flow with surface tension force is reasonably simulated. In the second and third cases, the validation is applied on the droplet deformation which proves that the current study has captured droplet deformation well and its breakup for the cases of high shear rates. In the fourth case, we have validated the main flow in which the hydrodynamic behavior of the global main flow is studied and compared completely. Finally a grid resolution study is checked to be sure that results are independent of the grid size.

3.1. Validation with analytical solution

We first simulate a droplet in a surrounded fluid in a periodic gravity-free domain which is very common for the cases of drop motion. Laplace law is used for measuring surface tension force, expressing that the pressure difference across the phase interface is linearly

proportional to the inverse of the droplet radius. Also, the slope of this line is the surface tension force. The Laplace law is expressed as.

$$\nabla p = p_{in} - p_{out} = \frac{\sigma}{r}, \tag{18}$$

in which, p_{in} and p_{out} refer to the fluid pressure inside and outside of the droplet, respectively, r is the radius of the droplet and σ is the surface tension coefficient. As it can be seen in Fig. 4, the results of the current study for the pressure difference in the Laplace law are compared with an analytical solution. Excellent consistency underlines the accuracy of the present simulation.

3.2. Drop deformation

In the second case, we consider droplet deformation in a simple shear flow generated by the motion of top and bottom walls with the same velocity in opposite directions, as illustrated in Fig. 5. This test case is very common when the droplet is exposed under high shear stress rate. The droplet deformation versus dimensionless time was compared with the numerical results reported by Sheth and Pazrikidis [65]. The simulation is conducted until a steady state shape is reached. The dimensionless parameters related to the deformation of a droplet in a shear flow are the viscosity ratio of fluids, λ, capillary number, $Ca = \frac{U\mu}{\sigma}$ and Reynolds number, $Re = \frac{\rho U(2R)}{\mu}$. The drop deformation parameter is $D_f = \frac{L-B}{L+B}$, where L and B are the maximum and minimum drop dimensions, respectively. As dimensionless time we use $t^* = tU/H$. Fig. 5 shows the configuration of the test case.

Fig. 6 illustrates the comparison of results of the current study with those by Sheth and Pazrikidis [65]. The physical properties of the test are $\lambda = 1, Re = 100$ and $Ca = 0.4$. The results of the current study are in very good agreement with those obtained in [65].

3.3. Drop deformation with breakup

Fig. 7 compares the deformation and breakup of a droplet in another test case with the results obtained by Farokhirad et al. [43]. This figure shows the breakup process for $Re = 10$. It can be seen that there is a good consistency between our results and the results gained by Farokhirad et al. [43]. The figure demonstrates that as the droplet is stretched it first gets an ellipsoidal shape. The minor axis shrinks while the major axis extends, which leads to the formation of a waist near the center of the droplet. Consequently, the droplet changes from an ellipsoidal shape to a dumbbell shape. Eventually a neck emerges between the central portion of the droplet and bulbs. It should be mentioned that the droplet radius in our study is 50 lattice units while it was 32 in the study by Farokhirad et al. [43].

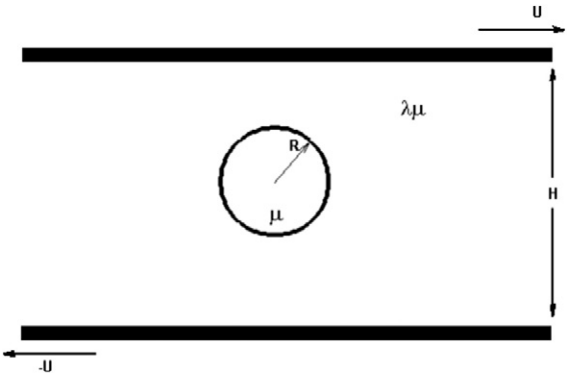

Fig. 5. Configuration of the test case according to [65].

3.4. Main flow validation

Applying the boundary conditions accurately is very important to simulate the flow physics correctly. To show that the boundary conditions are implemented precisely, the flow pattern in the main rotating flow and the centerline ***u***- and ***v***- velocity profiles in steady state for $Re = 1000$ and $\rho_h/\rho_l = 1$ are compared with the results reported by Ghia et al. [66] in Fig. 8. Since, when the density ratio equals one, there is no relative velocity between the main flow and the droplet, the flow pattern in steady state can be compared with the flow pattern in a standard cavity. The excellent agreement of the present results with those reported by Ghia et al. [66] demonstrates the accuracy and correctness of the implemented boundary conditions.

3.5. Grid dependency check

In another test case, to prove the grid independency, droplet deformation for $Re = 1000$ and $\rho_h/\rho_l = 5$ are illustrated in Fig. 9 for three different grid sizes, 250×250, 350×350 and 450×450, in three different positions in which the droplet experiences shear force and deforms. This figure demonstrates that the droplet shape simulated with a grid

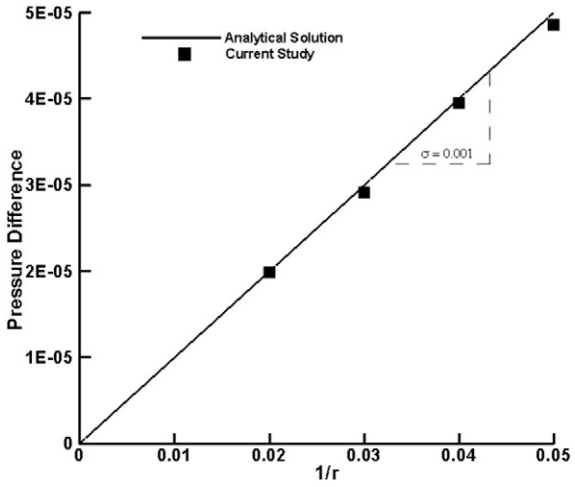

Fig. 4. Comparison of the current study results for the Laplace law for droplets with different radius.

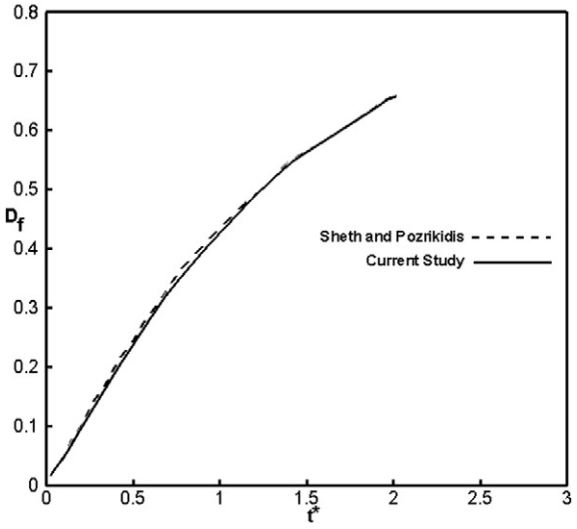

Fig. 6. Comparison of droplet deformation with the results reported by Sheth and Pazrikidis [65].

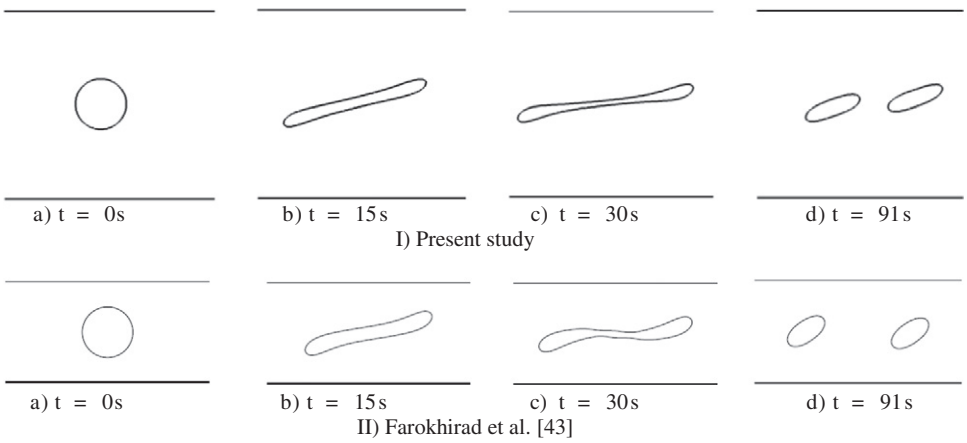

Fig. 7. Comparison of snapshots of droplet breakup for $\lambda = 1$, $Ca = 0.2$, $R = 50$ and $Re = 10$.

size 250×250 is slightly different from those obtained for the two other larger grid sizes. Also, the shapes of the droplet with grid sizes 350×350 and 450×450 are very close to each other. Based on this shapes, the present simulation is performed for the grid size 350×350.

4. Results and discussion

Droplet dynamics and the flow physics are extensively addressed in the three following parts: global flow physics, droplet deformation and droplet trajectories.

4.1. Global flow physics

In this section, the global flow physics is studied in detail. Also, relevant results reported by previous researchers, such as Xin and Megaridis [44] and Poon et al. [46], are presented here along with our studies done on rotating flow physics around a droplet.

A discussion on practical gas/droplet interaction within turbulent eddies was made by Xin and Megaridis [44] who considered a steady rotating or impulsively started, infinitely long, gaseous cylindrical container, Fig. 10. In their study, droplets were kept at

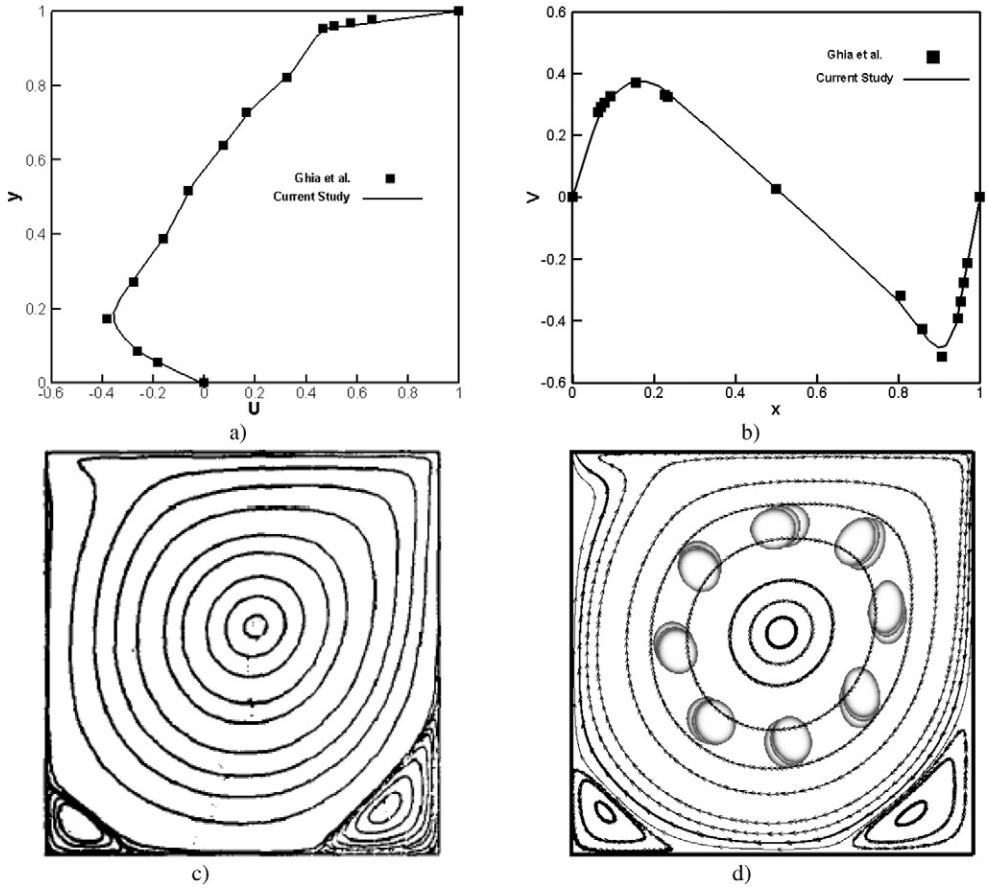

Fig. 8. Comparison of velocity profiles and flow pattern in rotating flow in steady state for $Re = 1000$ and $\rho_h/\rho_l = 1$ with the results in standard lid-driven cavity reported by Ghia et al. [66]; a) normalized of $\boldsymbol{u}$ — velocity component along vertical line through geometric center, b) normalized *of* $\boldsymbol{v}$ — velocity component along horizontal line through geometric center, c) flow pattern in standard cavity in steady state reported by Ghia et al. [66], d) flow pattern in rotating flow in present study.

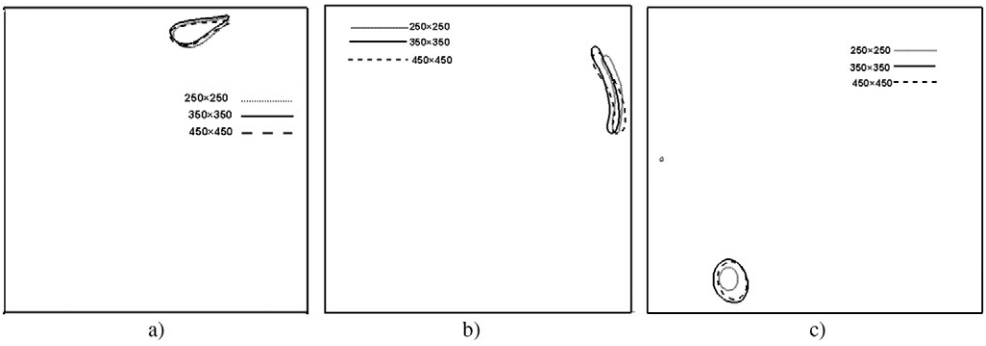

Fig. 9. Droplet deformation in rotating flow in three different positions for three grid sizes, 250×250, 350×350 and 450×450; $Re = 1000$ and $\rho_h/\rho_l = 5$, data of the present study.

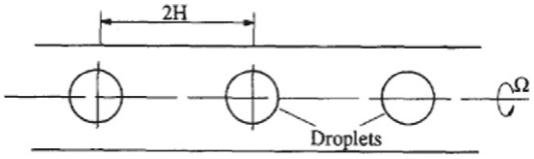

Fig. 10. Schematic of rotational flow configuration, according to [44].

the cylinder axes and could just turn around themselves without any translational motion.

Fig. 11 shows the influence of each droplet on its immediate vicinity in terms of iso-contours of the azimuthal velocity. Because the gaseous flow was considered a solid body rotation, the contour lines of the azimuthal velocity were initially parallel to the sidewall. After introduction of droplets, the azimuthal gas velocity component near the droplet surface was suddenly reduced by shear interaction with the quiescent liquid, case (a). As seen in this figure, the azimuthal velocity of both phases near the gas/liquid interface increased gradually, and the contour lines became increasingly flatter (compare cases (a) and (b)). Compared with the gas phase, the momentum diffusion within the liquid was much faster because of its higher viscosity; at $\tau = 24$ (τ was the dimensionless time, normalized with respect to droplet radius, minimum angular velocity, radius of cylindrical rotating tube and also stress) the azimuthal velocity contours within the droplet were almost parallel to the sidewall. This means that the rigid body rotation was being approached by the droplet [44].

The secondary motion in both phases is shown in Fig. 12 in terms of instantaneous particle path-line projections on the X-Y plane at four different instances. Because of the introduction of initially quiescent droplets, the azimuthal velocity of gas was reduced near the droplet surface, where the initial balance between the centrifugal and pressure forces was disturbed. The decrease of the centrifugal force induced the gas near the equatorial plane to move toward the axis of rotation, Fig. 12a. The secondary motion within the droplet was more complex. The liquid's secondary motion induced by the rotating droplet surface was still developing and was relatively weak. As the azimuthal moment was continuously transferred from gas to liquid, the strength of the secondary motion within the droplet was increased. A secondary motion in the opposite direction developed gradually, Fig. 12b. As time proceeded, the direction of the liquid secondary motion was gradually reversed and at later times, the momentum transfer within the droplet presided over the opposing surface shear stress, Fig. 12c. As the velocity distribution in the droplet approached the rigid body rotation, the strength of the induced secondary motion decayed and eventually died out, as indicated in Fig. 12d [44].

It should be noted that in Xing and Megaridis [44] work, since the droplets were at the center of an unidirectional rotating flow around the cylinder axis, therefore, they didn't have any translational

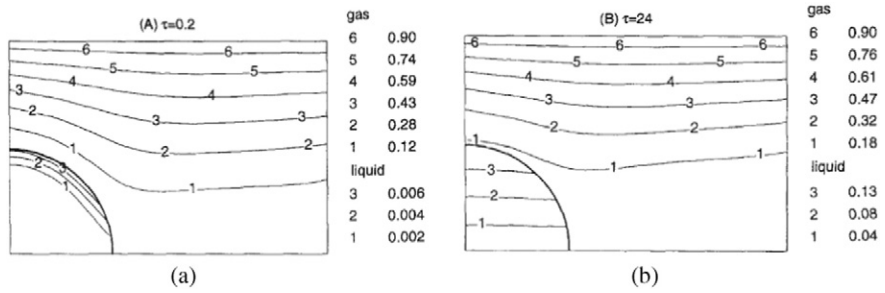

Fig. 11. Azimuthal velocity contours in the flow domain at a) $\tau = 0.2$, b) $\tau = 24$, according to [44].

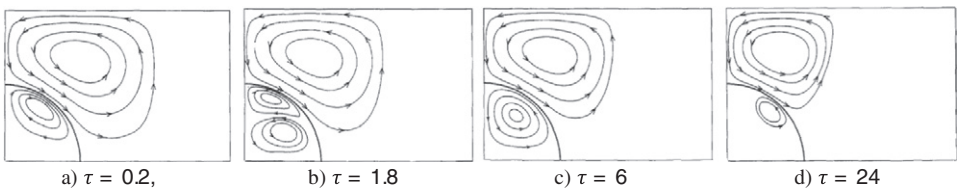

Fig. 12. Induced secondary (non-rotational) motion in both phases at four different instances, according to [44].

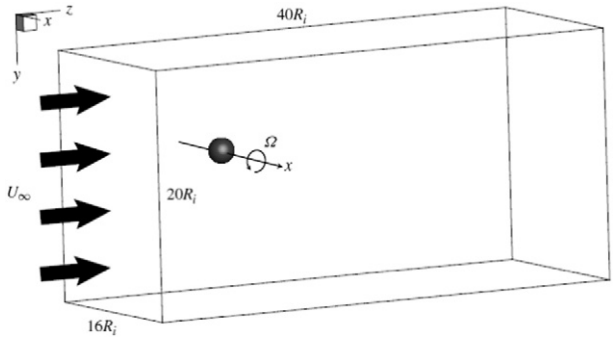

Fig. 13. Representation of the computational domain, according to [46].

motion from their initial position, rather they just had a spinning motion around the axial centre of the cylinder. Also, the droplets were assumed to be solid spheres and their deformation wasn't considered. So, there wasn't a real interaction between the droplets and the surrounding fluid.

Getting deeper knowledge about droplet dynamics, the results obtained by Poon et al. [46] are perused here. They have studied a rotational droplet in a uniform flow. They investigated the effects of transverse rotation on the dynamics of a droplet released into a uniform cross flow. As shown in Fig. 13, a spherical droplet of radius R_i with an initial angular velocity, Ω, in the x-direction was subjected to a sudden acceleration by a uniform free stream, U_∞, in z-direction.

Their results proved that for $\Omega^* \leq 0.2$ (Ω^* was the dimensionless rotation rate with respect to the initial angular velocity Ω, radius of the spherical droplet and uniform free stream) the transverse rotation led to droplet tilting as it was moved downstream. The tilting was a result of the vortex inside the droplet that was deformed and tilted by the uniform cross flow. In addition, the droplet was drawn and elongated toward the retreating side creating a positive lift coefficient. As the droplet evolved, a secondary vortex was formed across the upper lee side of the interface. This induced vortex elongated the droplet in the opposite direction and led to a negative lift coefficient. The lift coefficient was less affected by the droplet frontal area as it mainly depended on the velocity difference between the upper and lower droplet surface [46].

For $\Omega^* \geq 0.4$, the evolution of the droplet in the rotation-dominated regime and its deformation was specially different. In order to confirm that the increase in Ω^* had resulted a delay in droplet tilting, the streamlines in a moving reference frame for $\Omega^* = 0.6$ were plotted in Fig. 14. At $\Omega^* = 0.6$, the droplet deformation was directed by rotation effects due to a large rotation Weber number, $We_r = O(10)$. Here, the Weber number, density ratio and viscosity ratio are defined as $We = \frac{\rho_m (U_\infty)^2 2R}{\sigma}$, $\eta = \rho_d/\rho_m$ and $\lambda = \mu_d/\mu_m$, respectively. Also, the subscripts m and d refer to the surrounding flow and droplet, respectively. The radially outward expansion of the droplet helped to hold the unstable focus structure at the droplet centroid, as seen in Fig. 14b and c for a longer period of time. In addition, the unstable focus structure maintained its shape for a longer time and was only tilted and deformed after the droplet stopped contracting at its poles, Fig. 14d. The tilting and deformation of the vortex inside the droplet were the primary mechanisms responsible for the tilting of the droplet, and these mechanisms were delayed at $\Omega^* = 0.6$ [46].

Although, Poon et al. [46] gave a detailed discussion on spinning droplets in a uniform cross flow, their flow field was not rotating and did not contain any vortex or recirculating regions. Therefore, the spinning droplet was converted simply downstream. So, the droplet dynamics is completely different when it is considered in a complicated rotating flow as we discuss in this paper. In continuance, droplet dynamics in a rotating flow is explained in detail further below for three different density ratios: 1, 10 and 1000.

4.1.1. Density ratio 1

To have a better perspective of our study, flow physics in rotating flow is examined for density ratio one in Fig. 15. Since the density ratio of two phases is one, there is no relative velocity and the droplet moves with the same velocity as the main flow does. As it is expected, the global flow pattern is the same as the lid-driven standard cavity shown in Fig. 15. However, during time evolution of the flow in the cavity, the droplet is affected by the vorticity field. Consequently, the droplet is deformed, stretched and shrunk at different positions which are discussed here. At $t = 0.11$ s, a vortex is created near the top wall and the droplet is affected by the main rotating flow. At time $t = 0.18$ s, the main vortex grows and moves more toward the center of the cavity and the droplet has moved with the rotating flow toward the top wall while it is deformed. As the droplet moves by the main flow, it rotates and is affected by a velocity gradient field. Therefore, it experiences a large shear force stretching the droplet as shown at $t = 0.24$ s, 0.29 s and 0.33 s in Fig. 15. Another phenomenon that can be seen at $t = 0.29$ s is that a vortex is created beside the right wall which grew up and moved downward at $t = 0.33$ s. At $t = 0.33$ s, the droplet is aligned with the direction of the main flow. At this step, the droplet is located in a spatial accelerating ($t = 0.33$ s) and immediately decelerating flow field ($t = 0.38$ s). Therefore, it is stretched and shrunk from

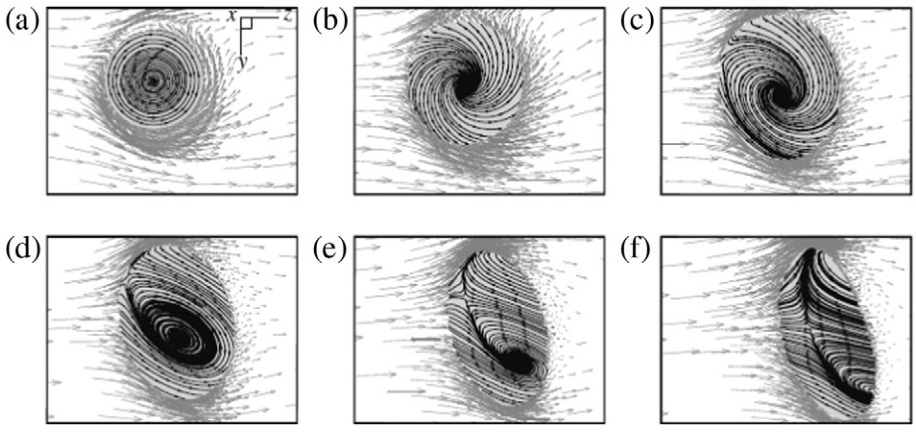

Fig. 14. Evolution of the velocity field inside an initially rotating droplet at $Re_i = 40$, $We_i = 40$, $\Omega^* = 0.6$ and $\eta = \lambda = 50$: (a) $t^* = 0$, (b) $t^* = 2.5$, (c) $t^* = 5$, (d) $t^* = 7.5$, (e) $t^* = 10$ and (f) $t^* = 12.5$. The shaded region represents the droplet cross-section area on the (y–z)-plane, according to [46].

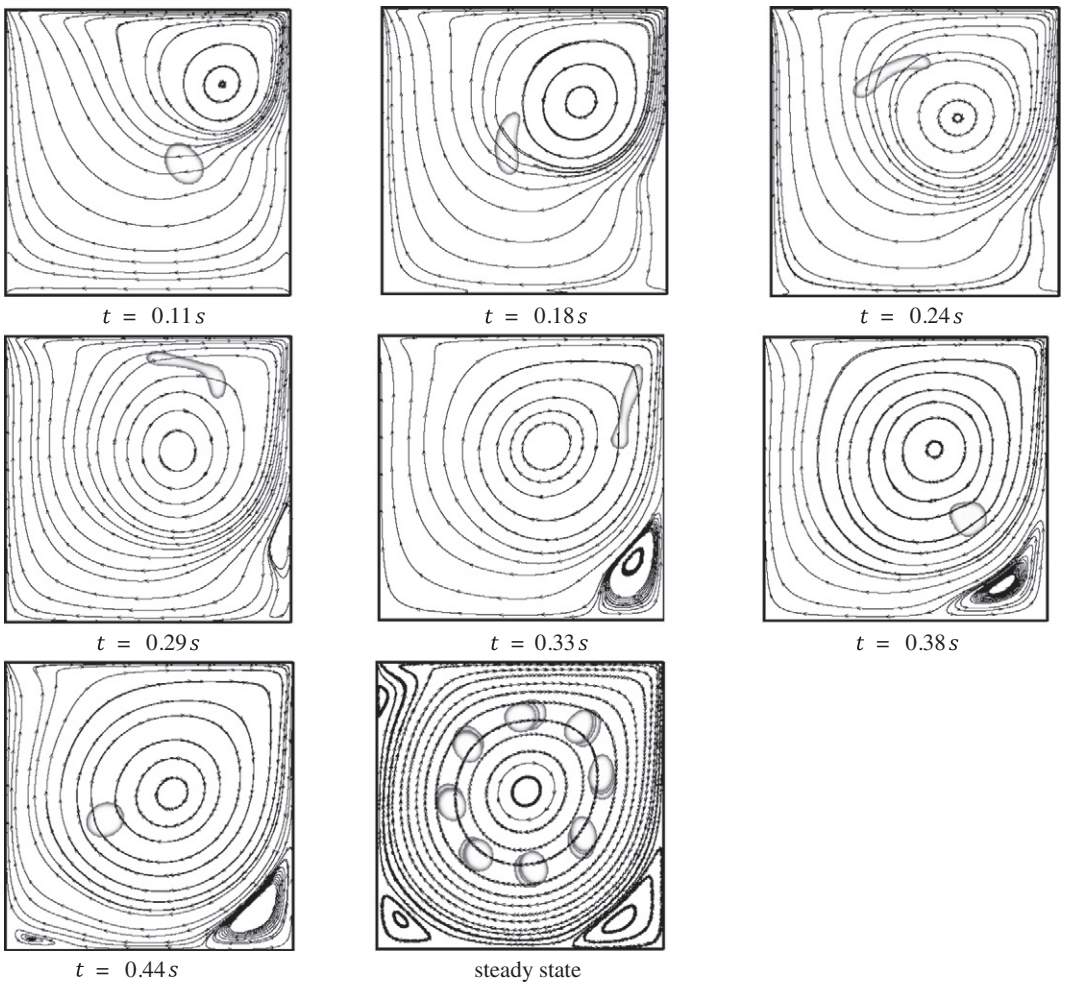

Fig. 15. Time evolution of flow pattern and droplet behavior in the cavity for $C = 0.5$ and $\rho_h/\rho_l = 1$, data of the present study.

rod shape to a circular shape, respectively. Also, at $t = 0.44$ s, another bottom vortex is created at the left corner, corresponding to the second vortex in the lid-driven cavity. Finally, when the flow field reaches the steady state, the global flow pattern behaves as a standard lid-driven cavity with a main big vortex and three small counter rotating vortices. At this situation, the droplet lies between constant streamlines. Hence, its shape remains unchanged while rotating at a constant radius around the center of the cavity. It should be mentioned that when the density ratio is one, the radius with which the droplet is rotating around depends on the initial position of the droplet and its size (will be discussed later).

4.1.2. Density ratio 10

To study different aspects of the flow pattern and droplet motion in rotating flow, time evolution of flow pattern and droplet behavior in the cavity are illustrated in Fig. 16. At the given density ratio, the drop is 10 times heavier than the surrounding liquid flow. The contour is plotted for C = 0.5 and the droplet begins to move from the center of the cavity. At first, the droplet moves in the direction of the flow and a vortex appeared in the top right hand side of the droplet, $t = 0.07$ s. By time, this vortex grows in size and the droplet moves toward the upper wall in direction of the rotating flow. Also, a small vortex is created in the right hand side of the drop near the wall. This is well seen at $t = 0.17$ s. Formation of this vortex is due to the change of the global flow physics by the droplet. This point is evidence by comparing Fig. 15 as a standard cavity and Fig. 16. The mentioned vortex disappeared at $t = 0.27$ s and the drop has gained an upper position. Since the densities of the two fluids are different, there is a relative velocity between them and the drop does not move with the same velocity as the surrounding flow does. At $t = 0.37$ s, the droplet reaches a position close to the upper wall and experiences some shear which leads to its deformation. A vortex appeared then in the right bottom corner of the cavity, too. This stretching and deformation is stronger at $t = 0.42s$ and the created vortex in the right bottom corner grew in size. The droplet tends to move with the same direction of the surrounding flow downward in a rod shape. At $t = 0.47$ s, the main flow in the cavity has changed some more and another vortex is created in the left bottom. Also, the droplet now came near the middle of the cavity with a shrunk shape. When the droplet gets to the lower wall the flow physics changes considerably. At this time, $t = 0.54$ s, the droplet acts like an obstacle in the main flow and a small vortex forms behind it and one of the bottom corner vortices disappears. This physics continues at $t = 0.56$ s and the droplet experiences more shear which causes to shape it like a rod, again. At $t = 0.59$ s, the droplet gained its previous shape with shrinkage and it behaved like an obstacle and caused a vortex to appear ahead of it. A corner vortex with two cores is formed in the right bottom corner and a young vortex appeared behind them, too. By letting time to pass, it can be seen that the droplet is rotated at $t = 0.61$ s and is moving upward. The two corner vortices at the bottom are formed again. While the droplet continues to move it reaches the left side of the rotating flow with an approximate spherical shape at $t = 0.73$ s. In this situation that the droplet has a density ratio greater than one, contrary to the droplet

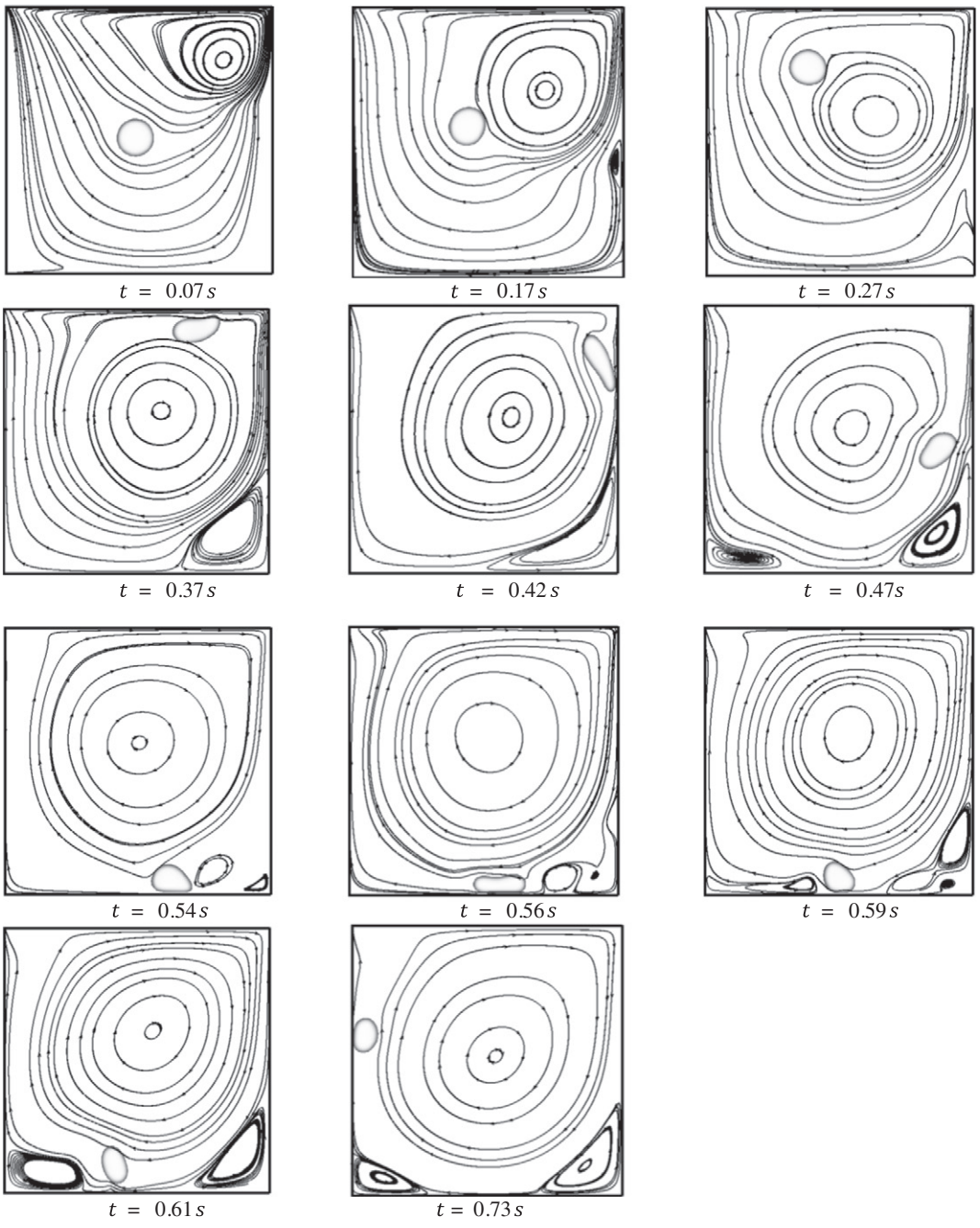

Fig. 16. Time evolution of flow pattern and droplet behavior in the cavity for $C = 0.5$ and $\rho_h/\rho_l = 10$,

with a density ratio of one, the droplet and the main flow will not reach a steady state but it continues to move without getting any steady state situation. It is worth mentioning that in all situations the droplet and the main flow have a relative velocity and the flow pattern is completely different from a standard cavity or cavities with obstacles on the walls [67].

4.1.3. Density ratio 1000

In another test case, a droplet is considered which has a density ratio 1000 times larger than the rotating flow around, Fig. 17. As this figure demonstrates the flow pattern changes dramatically and a chaotic pattern governs the main flow. In most situations, the main vortex of the rotating flow is affected by the droplet and this influence is great sometimes (see cases f, i and k). Also, in case j, a vortex is created in front of the droplet. Another point is that corner vortices in the bottom are formed from moment e, but their shapes change in each case and from case i this change becomes very obvious.

It can be understood that for this density ratio, the droplet behaves like a very heavy solid sphere. However, when there is a very heavy solid sphere, the flow will finally become steady while the flow is always unsteady here and this point is very important from a mixing point of view.

The motion and deformation of droplet at a density ratio of 1000 show that the droplet movement is very slow and its deformation is unnoticeable due to its high inertia. In comparison to the droplet the with density ratio of 1, it can be seen that droplets at high density ratios create an irregular pattern in the rotating flow while the rotating flow surrounding a droplet with a density ratio of 1 behaves like a standard cavity.

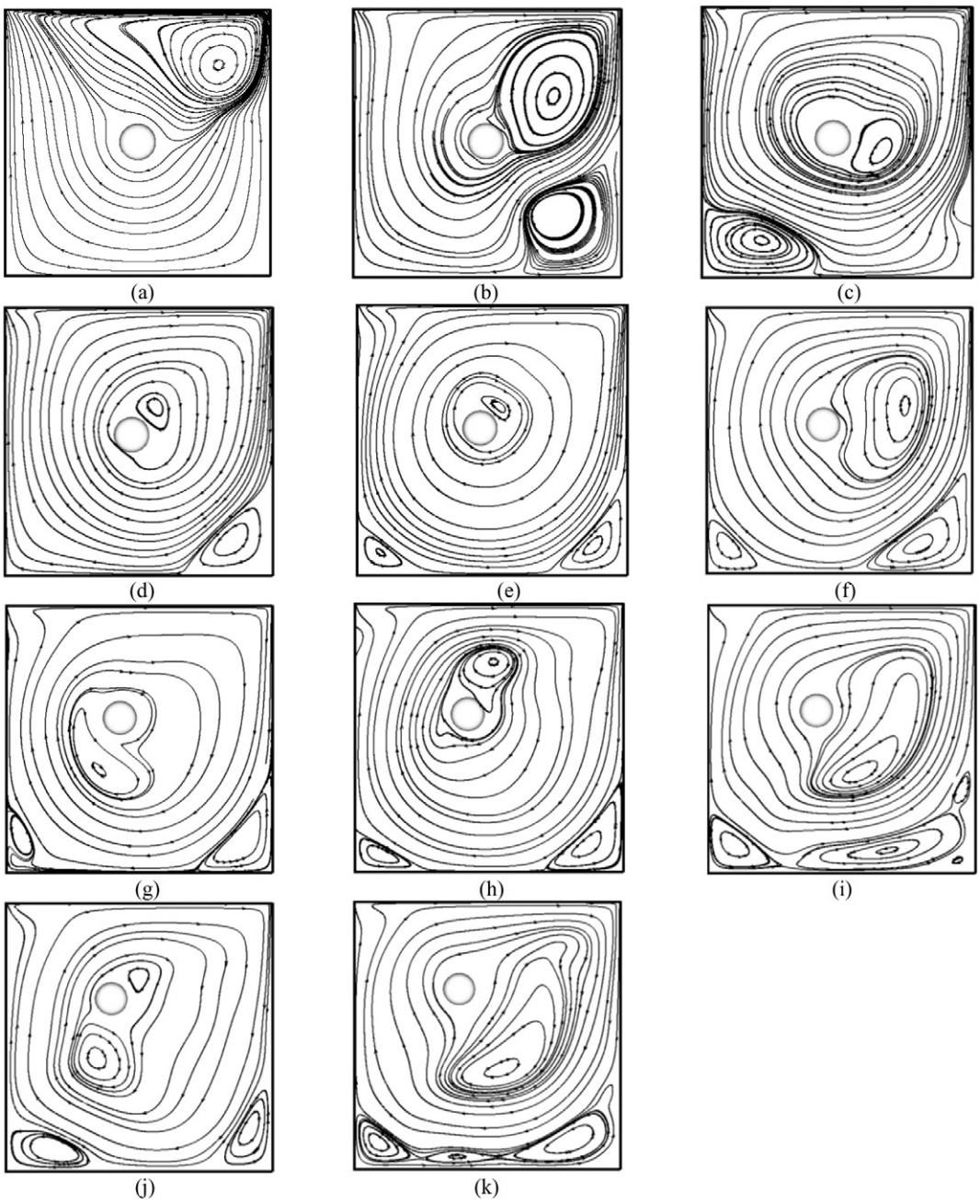

Fig. 17. Flow pattern and droplet behavior in the cavity for $C = 0.5$ and $\rho_h/\rho_l = 1000$, data of the present study.

Also, the droplet motion for different density ratios at different times and locations are compared in Fig. 18, while the initial positions of all drops are the same. The physics that governs in this figure is that for a density ratio of 1 there is no relative velocity between the rotating flow and the droplet. However, by increasing density ratios, there would be a difference between the drop's speed and the main flow velocity. The higher the droplet density ratio is, the higher is its relative velocity difference. Consequently, heavier droplets move slower than lighter ones, because of their higher inertia. Hence, they have different pathlines and deformation rates. At $t = 0.2$ s, the droplet with density ratio 1 has stretched much and moved, but the other two droplets have not moved much or deformed, especially for $\rho_h/\rho_l = 10$. Another point that should be mentioned is that a droplet with $\rho_h/\rho_l = 1$ moves toward the center of the rotating flow while others move toward the wall because of the centrifugal force. This phenomenon is obvious at $t = 0.37$ s. At this time, the droplet with a density ratio of 5 is located in an accelerating zone and is stretched, while the one with a density ratio of 10 is starting to pass the accelerating zone and has not deformed much. Also, at $t = 0.56$ s, when the density ratio is 5, the droplet experiences a decelerating zone while the one with a density ratio of 10 experiences an accelerating zone.

It can be concluded that droplets with a higher density ratio will move slower which is distinctive from the distance that droplets move in a specified time. Also, droplets with different density ratios will move in different pathlines depending on their density or inertia. Another point which should be noted is that droplets with higher density ratios will resist more against deformation.

4.2. Droplet deformation

This part discusses droplet deformation in a rotating flow, based on results reported by Poon et al. [46], Egholm et al. [45] and

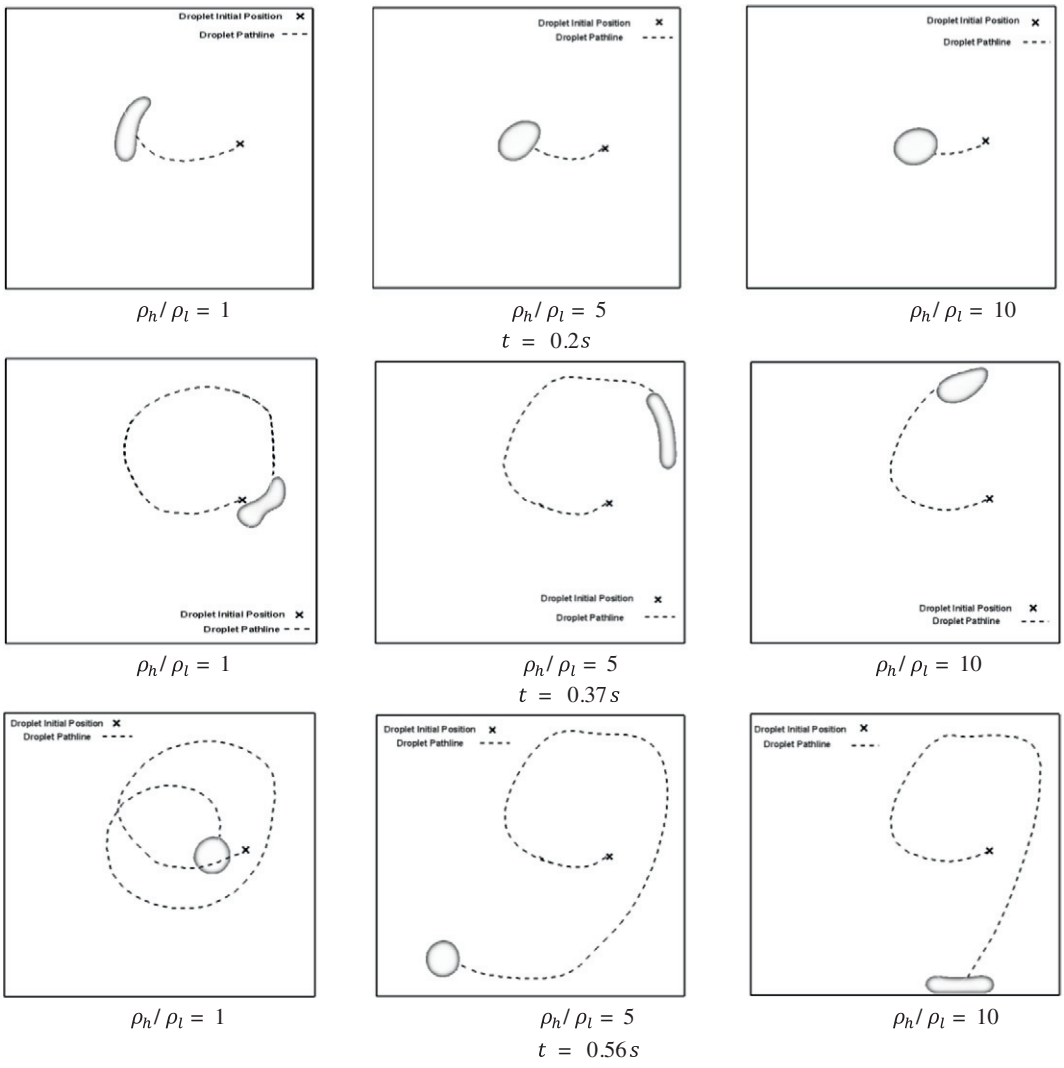

Fig. 18. Comparison of dynamics of droplets with different density ratios at different times: $C = 0.5$, data of the present study.

Qiao et al. [56]. As mentioned before, the research performed previously by others differs considerably with the present study. This will be explained more when discussing their results. Our aim is to develop a fundamental perspective about droplet dynamics in somehow rotating flows.

As mentioned, Poon et al. [46], studied a rotational droplet in a uniform cross flow and demonstrated that when Ω^* was small, the droplet was compressed by the free-stream inertia. The droplet deformed into an oblate spheroid at early times of droplet evolution, with both the upwind and lee side of the droplet being continuously flattened. In later stages of the simulation, the deformation of the upwind side of the droplet became slower while the lee side smoothed. The droplet remained axisymmetric in the azimuthal direction throughout the entire simulation time [46].

At $\Omega^* = 0.4$, there was a notable change in the droplet evolution at earlier stages. The compression of the droplet along the rotation axis became more distinguish; the flattening of the droplet was linked to the radial expansion of the droplet normal to its rotation axis. Also, it was obvious that expansion of the droplet normal to the rotation axis slowed down and the droplet became tilted. As the droplet expanded radially, the tangential interface velocity decreased in order to conserve the angular momentum. This reduction in tangential velocity may also be attributed to the transfer of rotational kinetic energy from the droplet to the surface energy at the interface. As the rotational kinetic energy lessened, the droplet stopped expanding and the free-stream effect dominated and compressed the upwind side of the droplet, which resulted in the occurrence of a small depression, D. The dominating free stream created a flat upwind interface whereas the history effect of the droplet rotation compressed the lee side of the droplet along the rotation axis, creating a depression as shown in Fig. 19b. The evolution of the droplet at $\Omega^* = 0.6$ showed a similar trend $\Omega^* = 0.4$, except that the droplet was extended further away from the rotation axis due to the higher rotational velocity. As the droplet spun further away from the rotation axis, the surface tension at its edge increased and prevented further deformation at its edge and took a biconcave shape. As the depression appeared while the centrifugal force was still expanding the droplet, this depression occurred mainly due to the droplet rotation instead of the presence of a free-stream momentum. The tilting of the droplet was also delayed due to the stronger rotation, which kept the droplet expanding for a longer period. A further increase of Ω^* to 0.8 and 1 increased the centrifugal force such that the droplet became biconcave in shape, Fig. 19a, at earlier stages compared to $\Omega^* < 0.8$ [46].

It is worth to note that the droplet in a Taylor–Couette flow or in a simple uniform flow, [46] does not have a high degree of freedom for motion. So, its dynamics and deformation change dramatically

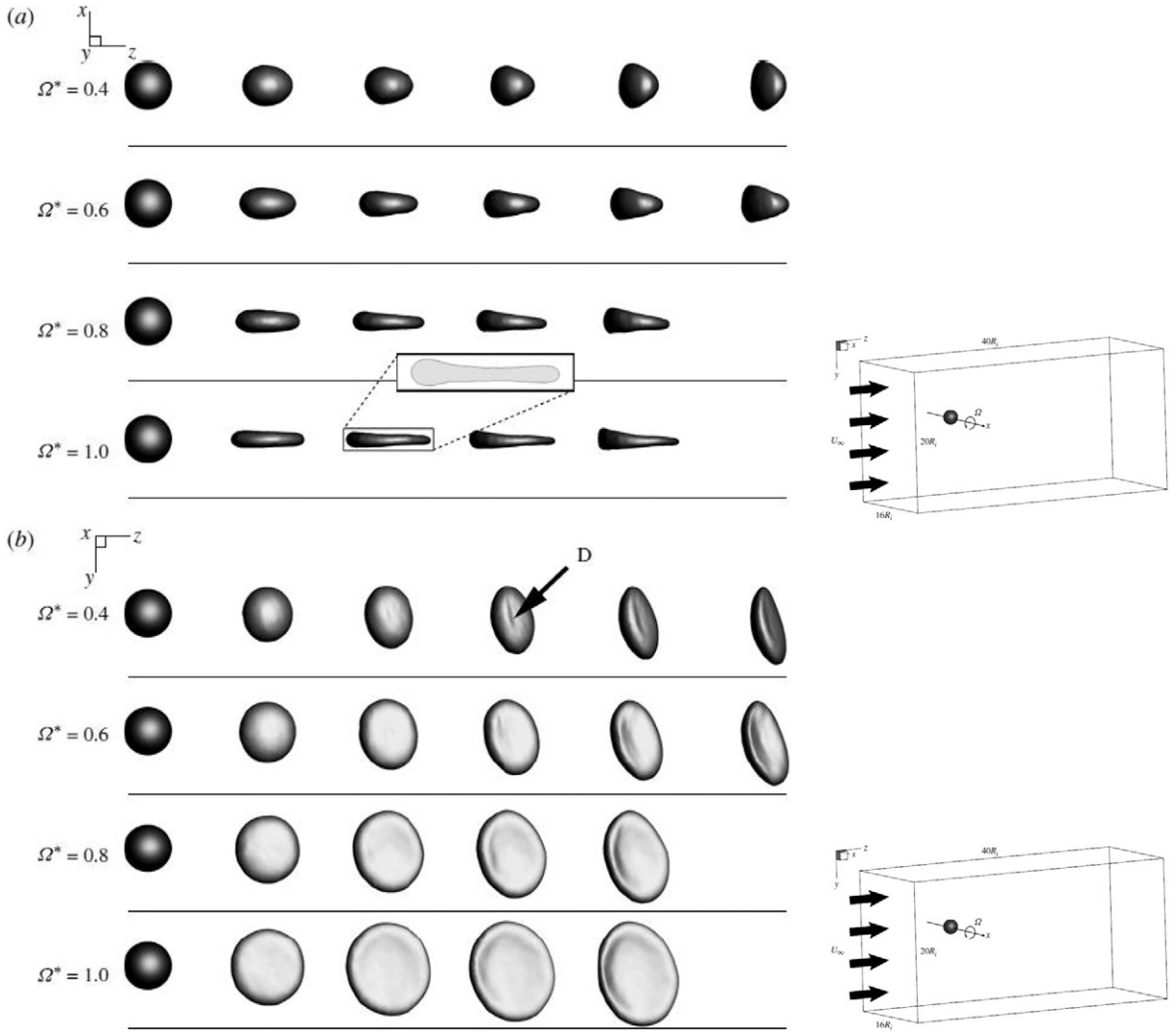

Fig. 19. Instantaneous droplet shape for $Re_i = 40$, $We_i = 40$, $\eta = \lambda = 50$ and $\Omega^* = 0.4$. The snapshots are shown at dimensionless time t^*, from left to right, of 0, 2.5, 5, 7.5, 10 and 12.5: (a) (x-z)-plane and (b) (y-z)-plane. D is the depression of the interface due to the combined effect of free stream and rotation, according to [46].

compared with our study here in which the flow field is highly complicated with the presence of different vortices and high shear region.

Fig. 20 presents the deformation of a droplet in a rotating flow when the density ratio is 1. Also, this figure compares droplet dynamics for different initial locations. The sequence of the numbers in these figures presents the location of the droplet in consecutive times. In Fig. 20a, the droplet initial location is at the center of the cavity. Since here the density ratio is 1, there is no relative velocity between the droplet and the carrying main flow. Therefore, the dropt follows the main flow pathline. However, the size of the droplet is such that it lies between vorticity fields of different strengths. Consequently, depending on the forces exerted on the droplet, it can tilt, stretch, shrink and sometimes breaks it up. For instance, as the droplet moves in the rotating flow, it stretches and deforms when it goes near the upper wall (positions 4, 5 and 6). Thereafter the droplet shrinks. In positions 8 and 9, near the right wall, the droplet experiences a strong shear due to the accelerating flow, gets stretched and deforms into a rod. Again, in position 10, the droplet moves away from the right wall and looks more like a small bean than a rod due to the deceleration. Finally, the droplet rotates and goes back to its circle shape.

To see the effect of the initial position on the droplet dynamics and its deformation, three other cases were considered where the initial positions of the droplet were 1/8, 2/8 and 3/8 of the cavity length out of the cavity center toward the right wall (cf. Fig. 20b to d), respectively. Comparison of the figures proves that the initial position of the droplet has an enormous influence on the droplet dynamics and its deformation because the pathline that guides the droplet is highly dependent on it. Therefore, droplets with different initial positions pass different regions where different shear forces are exerted on it. This is why the droplet in case c has a completely different shape than in the other cases. Indeed, it has been in a pathline that experiences high shear force while in case b it does not. On the other hand, the droplet in case d is located in a position which it experiences a gradual shear force leading to a smooth gradual deformation with respect to case c. It should be noted that among the cases a to d, the droplet which is passing through case c has the highest surface to volume ratio in the carrying flow which is very important from the point of view of property exchange between the two-phases; for example, exchange of mass and concentration.

As mentioned before, when the droplet density ratio is 1, the droplets will reach into a steady state and will rotate on a specified pathline starting from the initial position. Fig. 21 shows the steady state of the droplets for the three cases of Fig. 20a to c. There are three important points in their motion that should draw our attention: i) the shapes of the droplets are the same and spherical-like in all three cases which

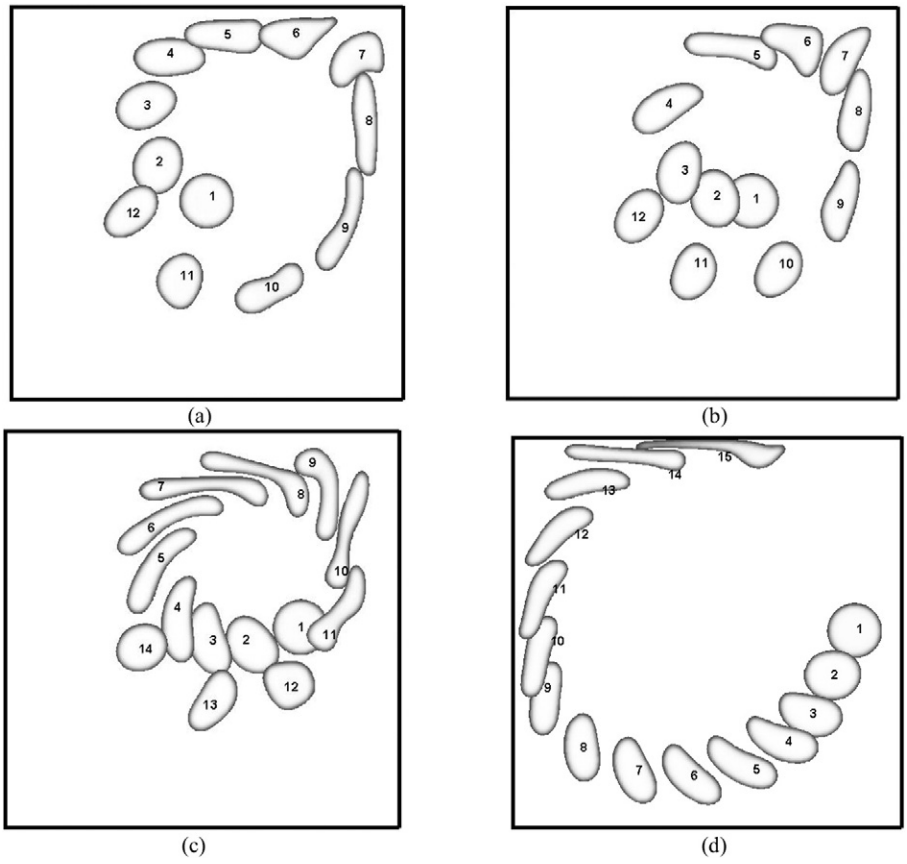

Fig. 20. Deformation of a droplet in a rotating flow with different initial positions: $C = 0.5$ and $\rho_h/\rho_l = 1$, data of the present study.

means that the droplets are in a flow field where they do not experience any relative shear force and just rotate. That is why they save their approximate spherical shape, ii) the droplets move in a constant radius and iii) this constant radius depends on their initial position, such that when the initial position of the droplet is closer to the center of the cavity, its rotating radius is smaller.

Among the researchers investigating droplet deformation, Egholm et al. [45] have studied the droplet deformation rate in a unidirectional flow without any report on droplet deformation itself. They studied the deformation rate of a single droplet suspended in a liquid in which the flow was generated in a rotor-stator device consisting of two concentric cylinders with teethed walls. Fig. 22 illustrates the deformation of the droplet versus time. Furthermore, the configuration of the cylinders and the droplet position in the channel were shown at three experimental times. The figure shows that a maximum deformation happened when there was a local minimum in the gap width and that the maximum deformation (last peak) was obtained when the gap width was close to the global minimum [45].

In another research, Qiao et al. [56] made an experimental study on droplet deformation in a semi unidirectional flow in which the droplet deformation is not sensed much and only oval stretching of the droplet can be seen. While in the present study, the droplet is exposed into a complex rotational flow and experiences different deformations passing through different regions. By detail, Qiao et al. [56] performed an experimental study on the behavior of individual droplets in a Taylor vortex of an immiscible surrounding fluid, a mineral oil with density of 0.86 g/cm^3 and viscosity of 0.066 Pa s. The behavior of the droplets was investigated with a high speed camera and a phase Doppler particle analysis (PDPA) system. Again, here, the droplet deformation was studied between two concentric cylinders in which the flow physics is like a simple one-dimensional flow and the droplet does not pass through any complex flow field, so that the droplet dynamics and

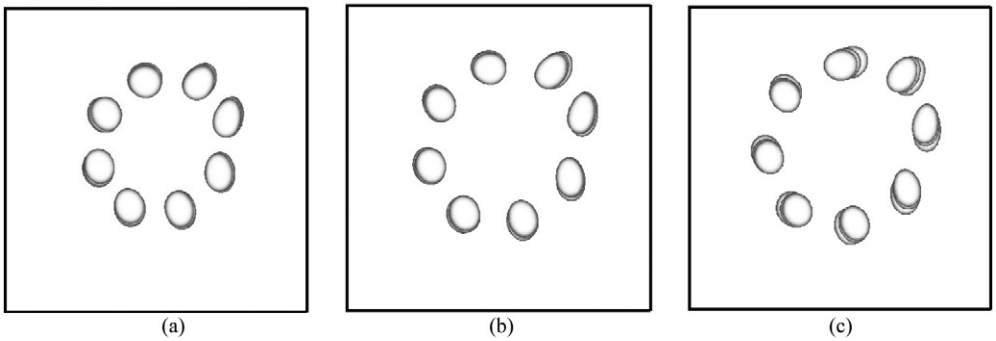

Fig. 21. Final position of droplet in a rotating flow with different initial positions: $C = 0.5$ and $\rho_h/\rho_l = 1$, data of the present study.

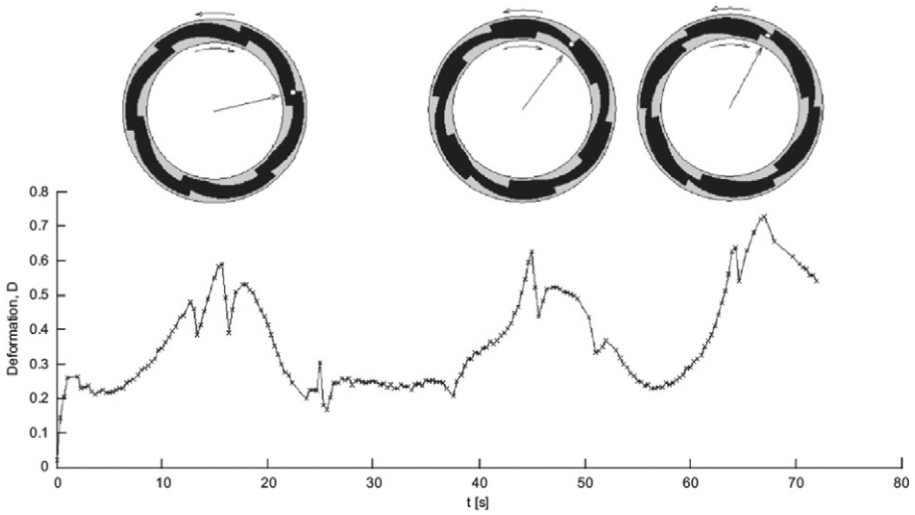

Fig. 22. Plot of drop deformation as a function of time. Also, shown is the configuration of the system and the drop position (white dot) at three experiment times. The arrow originating from the cylinders indicates the location of the drop, according to [45].

deformations are not complicated. The deformation of the droplet when moving along the annulus is demonstrated in Fig. 23. In all cases, the droplets showed ellipsoidal shaped orbits, with the major axis aligned along the moving direction. Compared to the spherical shape, such morphology was considered to pose minimal resistance to the motion of droplet. On the other hand, the shear stress experienced by the droplet varied at different locations and, therefore, the droplet morphology showed a periodic change correspondingly [56].

To have a better examination on the droplets behavior, their dynamics at a density ratio of 5 is studied here. Fig. 24 tracks a droplet motion in a rotating flow at different initial positions of the droplets. Since the density ratio of the droplet is larger than 1, the droplet and the carrying flow do not move with the same velocity and the same direction but the droplet crosses the carrying flow streamlines. This fact is because of the centrifugal force that moves the droplet out of the main streamline passing from the droplet position (cf. Fig. 24c). Therefore, the droplet will move away from its initial position in a spiral way. It should be mentioned that here the buoyancy force, due to the difference of pressure distribution around the droplet surface, is unnoticeable in comparison to the centrifugal force.

Also, due to the higher density ratio of the droplet, its initial inertia is larger and has the tendency to save its initial shape in

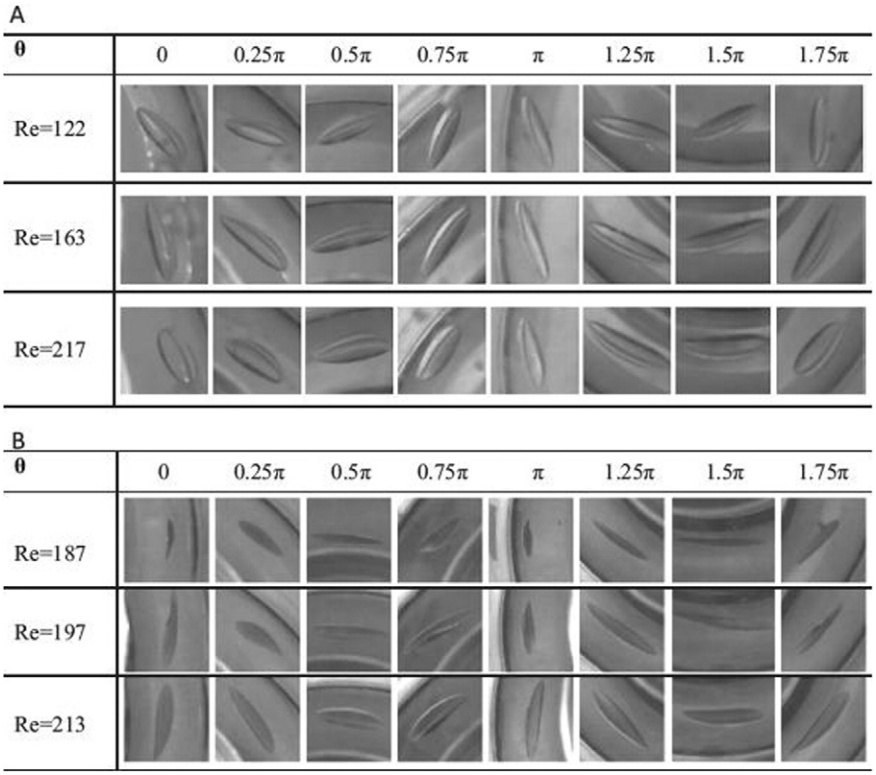

Fig. 23. Deformation of water droplet (A) and an ethanol droplet (B) studied at different angles in the annulus of a mineral oil. The snapshots were taken from the bottom, according to [56].

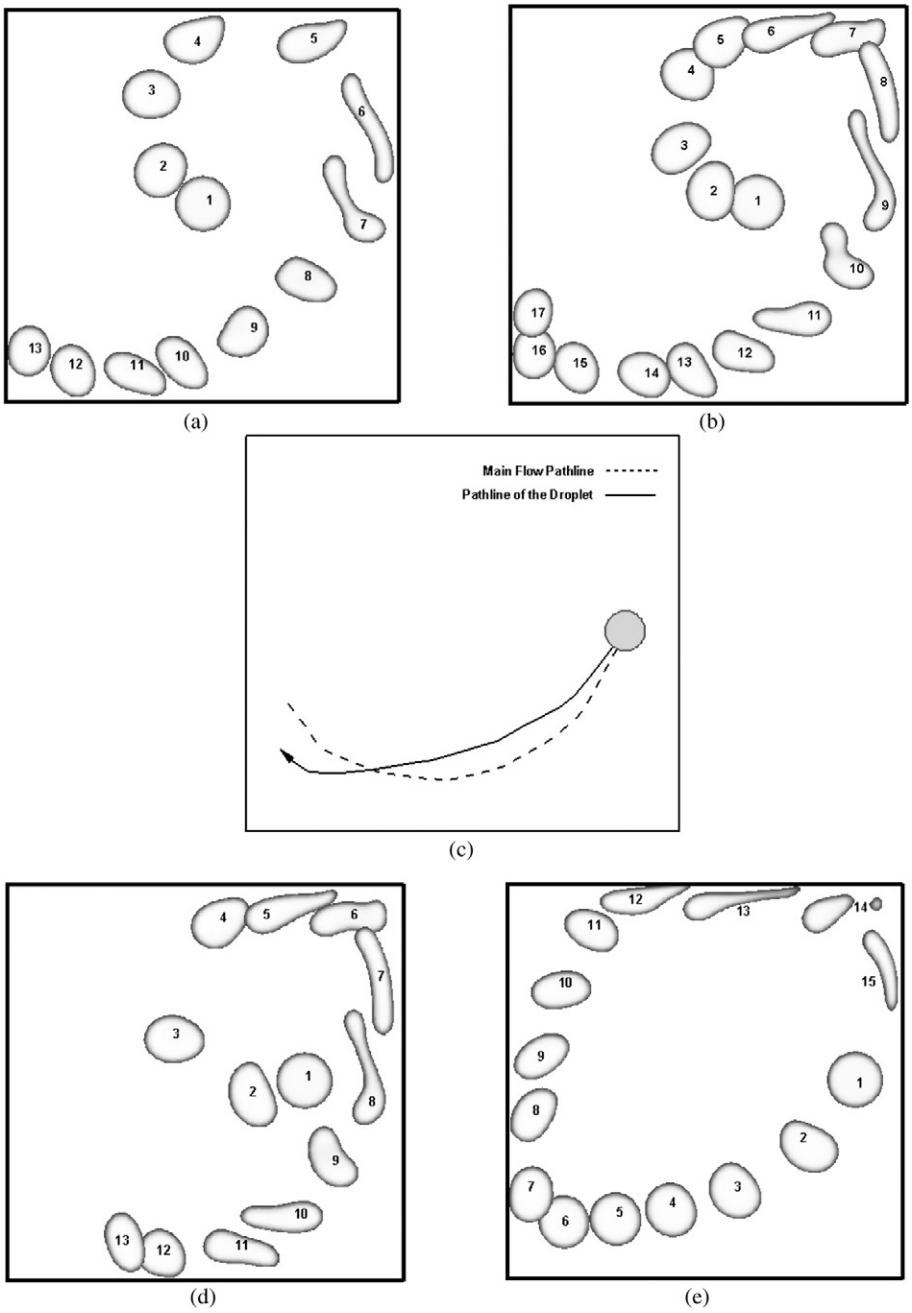

Fig. 24. Deformation of a droplet in a rotating flow with different initial positions: $C=0.5$ and $\rho_h/\rho_l=5$, data of the present study.

comparison with the droplet at the density ratio of 1. This large inertia causes the droplet to resist against deformation or movement and saves their spherical shape. This fact is more obvious when the density ratio is 10 (see Fig. 25). In addition, when the density ratio of the droplet is larger than 1, the centrifugal force on the droplet increases with time, which means that the final position of the droplet cannot be identified. It should be mentioned that the sequence of the numbers in these figures present the location of the droplet in consecutive times.

In order to study the droplet dynamics and its behavior in more detail, a droplet with a density ration of 10 is considered in Fig. 25. The corresponding droplet behavior shows that with increasing inertia of the droplet its deformation decreases and it can save its approximate spherical shape in most positions. Also, the droplet dynamics shows that whatever the density of the droplet increases, the mass or inertia of the droplet increases. On the other hand, the increase in density leads to a decrease of the absolute velocity of the droplet with the power of two. A simultaneous action of these two parameters results in a more intensive deviation of the droplet from the main flow streamline, as we can see in Fig. 25c. On the other hand, comparing Fig. 25 with Fig. 24 we can see that the droplets with higher density will deform less due to their higher inertia. For example, in Fig. 24e, the droplet has broken up into two parts in the accelerating zone because of the exerted large shear force while in Fig. 25e, the droplet has deformed to some extent. This fact is even more significant for the data shown in Figs. 25 and 20.

4.3. Droplet pathline

Let us now discuss the pathline and trajectories of droplets in a liquid flow field. The results of Arkhipov et al. [47] and Qiao et al. [56] are now analyzed here. Arkhipov et al. [47] performed a numerical study on

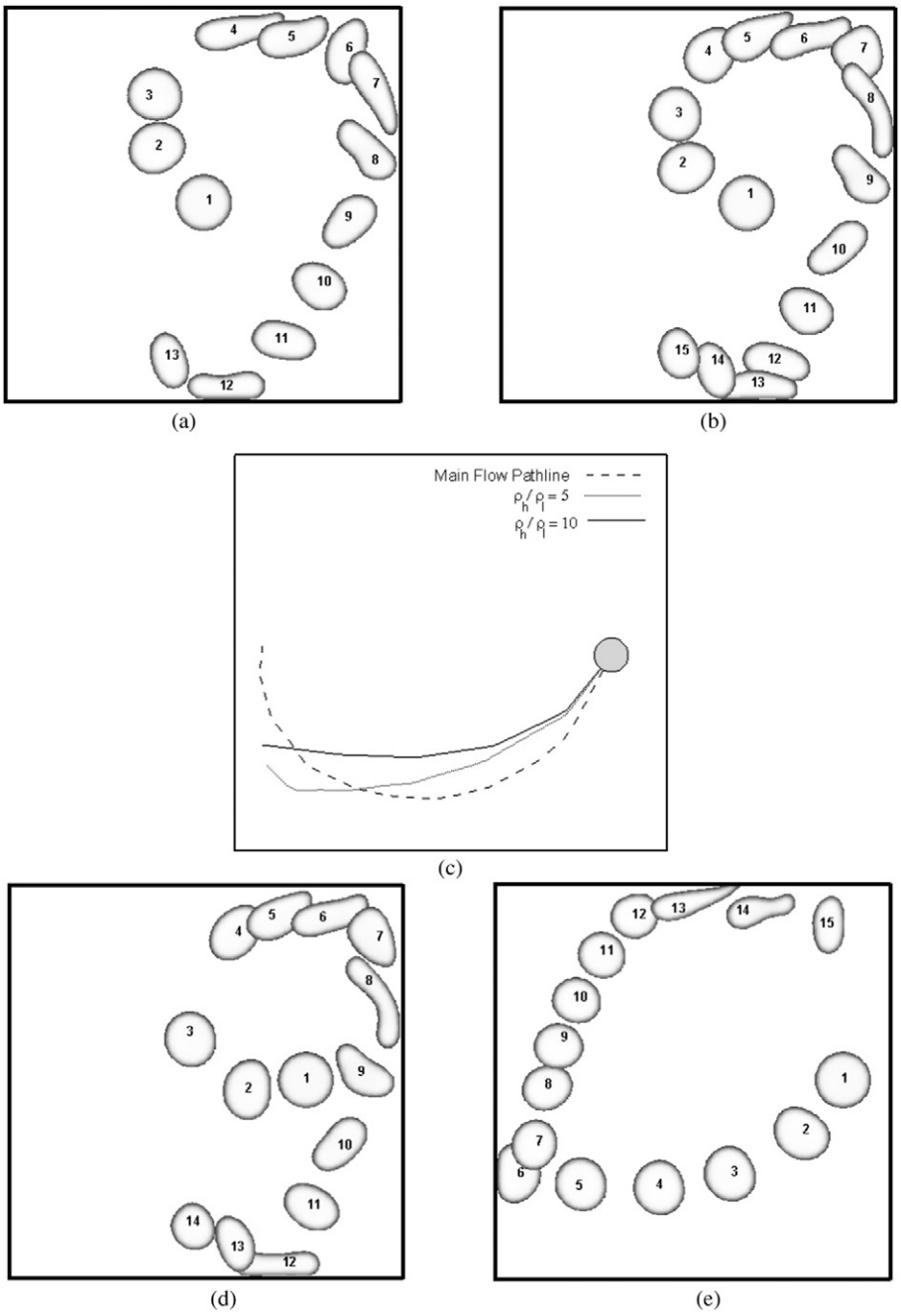

Fig. 25. Deformation of a droplet in a rotating flow with different initial positions: $C = 0.5$ and $\rho_h/\rho_l = 10$, data of the present study.

droplet dynamics by reporting droplet trajectory without any results of its deformation. However, in the present study, droplet dynamics is studied by detailed perusing of droplet deformation, its trajectory and global flow physics. Arkhipov et al. [47] determined the motion trajectory of a droplet, the axial, radial and tangential components of its velocity vector and similarity numbers in a twisted flow. The motion trajectory of the droplet (Fig. 26) was a spiral expanding in the direction of the *Oz* axis. The form of the spiral depended on the experiment parameters, in particular, on the droplet diameter. Fig. 27 illustrates the motion trajectories of different sized droplets in the projection onto a plane perpendicular to the rotation axis. Large-diameter droplets got to the reservoir periphery faster than smaller ones. With increasing viscosity of the surrounding liquid, the time for the liquid to get to the periphery of the reservoir increased (Fig. 27).

In another work by Qiao et al. [56], the authors have studied water and ethanol droplets trajectory in a mineral oil. In their study, they have investigated only droplet trajectory without considering droplet deformation or its complete dynamics. Fig. 28 shows the trajectories of water and ethanol droplets in the annulus studied by Qiao et al. [56] at different Reynolds numbers. Here *X* and *Y* were the two displacement components taken from the center of the inner cylinder normalized by the radius of the outer cylinder, respectively. For low Reynolds number, the water droplet was trapped near the vortex center, with equal distance to the center of the inner cylinder at any time. Therefore, the 2-D trajectory of the water droplet captured from the bottom was a circle (Panel A). For higher Reynolds numbers, the water droplet showed a three-dimensional toroidal motion along the annulus. As a result, the bottom view of the droplet trajectory had the shape of an

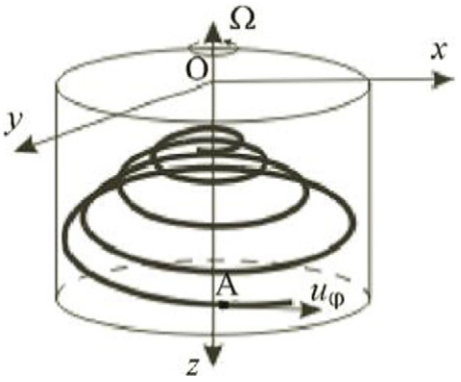

Fig. 26. Trajectory of droplet motion, according to [47].

ellipse as shown in Panel B. This motion continued for higher Reynolds numbers. The evolution of the ethanol droplet trajectory with increasing Reynolds numbers followed a totally different trend. For example, when the Reynolds number was 122, the projection of the droplet trajectory on the horizontal plane was an oval orbit (Panel D). At a Reynolds number of 213, the droplet was trapped at the vortex center and therefore its trajectory along the annulus was a circle (Panel F) [56].

In the present study, the determined droplet trajectories for different density ratios and initial positions are presented in Figs. 29 to 31. The initial positions of the droplet are marked with "×". For a density ratio one of 1, the pathline of the droplet and the main flow are the same and the droplet moves with the pathline of the carrying flow. Meanwhile, as was mentioned before, by increasing the density ratio, due to the higher inertia of the droplet and centrifugal force, it would not go through the pathline of the main flow; the higher the density ratio, the larger is the deviation from the carrying flow pathline, e.g. $\rho_h/\rho_l = 10$. In addition, as the density ratio increases, the droplet will get closer to the wall and it would be affected by the wall. This phenomenon is similar to the fact that an aerodynamical body is flying toward the ground and is affected by ground effects. Therefore, in high density ratios, the droplet will get closer to the wall, and would be affected by the ground such that a lift force resulting from an increasing pressure between the droplet and the wall will be exerted on the droplet and forces it to go away from the wall. This phenomenon is illustrated well in Figs. 25a–c and 31.

Another parameter which is analyzed here is the effect of the droplet diameter on its pathline. In Fig. 32, the pathline of four droplets corresponding to a density ratio of 100 and different diameters are compared. Increasing the droplet diameter means increasing the droplet mass or inertia which in turn increases the relative velocity between the droplet and the main carrying flow or decreases the absolute velocity of the droplet and its pathline radius. The centrifugal force exerted on the droplet depends on two important factors: droplet mass and its absolute velocity. As mentioned before, by increasing the density ratio, the droplet mass would increase and the resulting centrifugal force, too. On the other hand, increasing the density ratio means the absolute velocity will decrease and also, the decrease of the centrifugal force with the power of two, mV^2/R. Therefore, as an outcome, the more the diameter increases, the more decreases the centrifugal force. As a result, the droplet of larger diameter will experience the centrifugal force less and will move in a pathline with a smaller radius, e.g. $D/L = 0.2$.

5. Summary

This paper discusses the droplet dynamics and its complexity in a rotating flow, including the physics of the rotating main flow, droplet deformation and droplet trajectories. It is shown that at a density ratio of 1, there is no relative velocity between the droplet and the main carrying flow and the droplet moves with the same velocity as the main flow does. The pathline on which the droplet is moving is the main flow pathline starting from the initial position of the droplet. However, with increasing time of the rotating flow, the droplet is affected by the vorticity field and finally when it reaches the steady state the droplet lies between constant streamlines of the main flow. Hence, its shape remains unchanged while rotating at a constant radius around the center of the cavity depending on its initial position.

By increasing the density ratio, the global flow physics becomes affected by the droplet. Since the densities of two fluids are different, there is a relative velocity between them. Here, due to centrifugal forces, the droplet is thrown toward the wall by the main flow. At higher density ratio of the droplet, the initial inertia is greater and has tendency

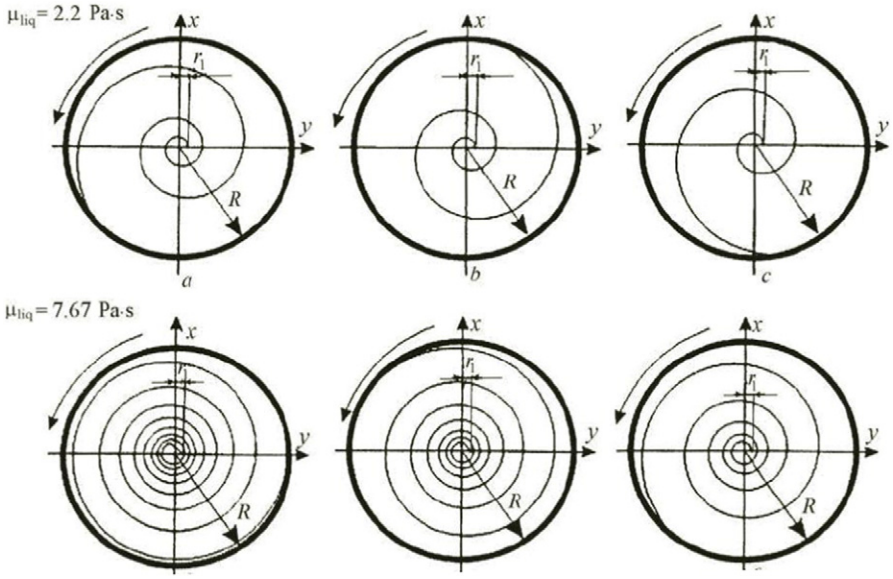

Fig. 27. Droplet motion trajectory at $n = 5.7$ rps; a, d) $D = 4$ mm; b, e) 4.5 mm; c, f) 5.3 mm, according to [47].

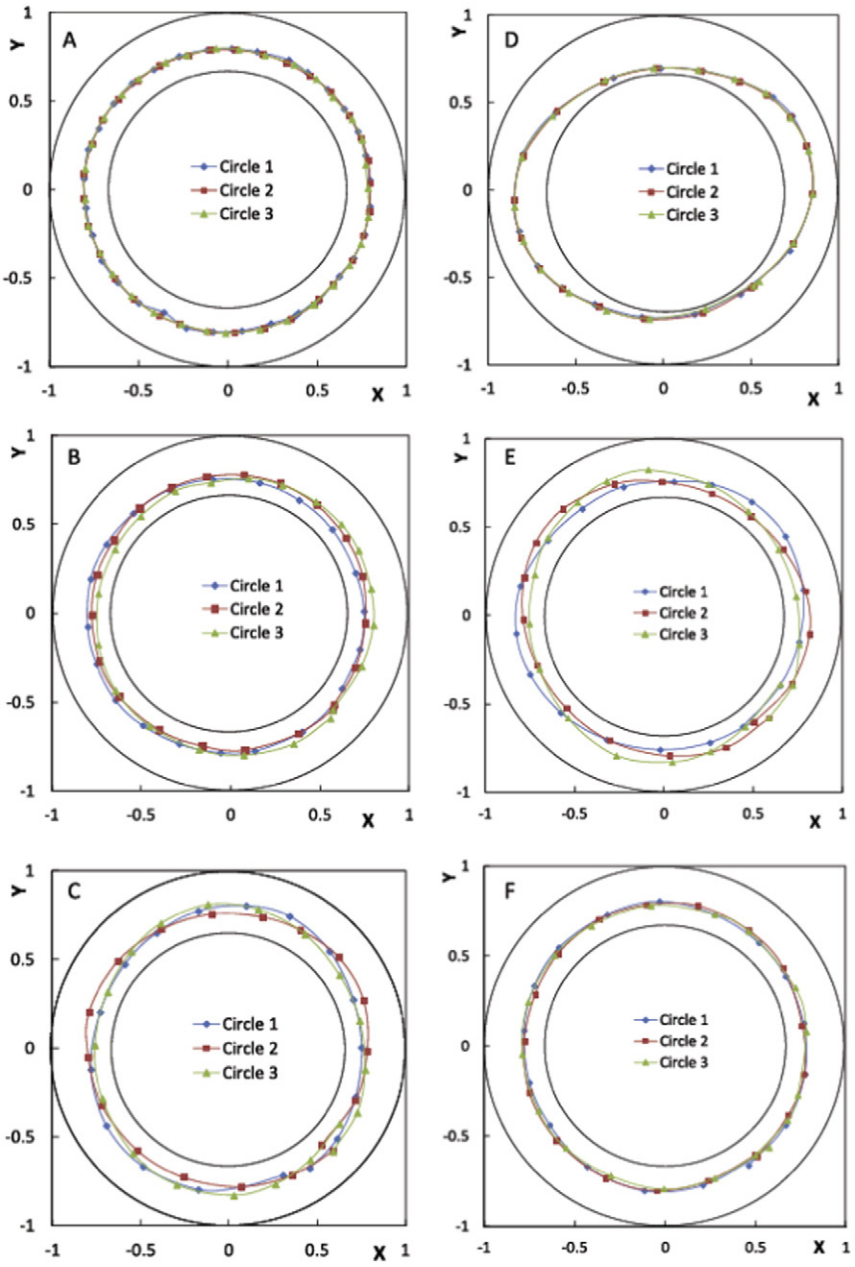

Fig. 28. Trajectories of water droplet (A–C) and ethanol droplet (D–F) in a Taylor vortex (bottom view) both in a mineral oil. (A) Re = 122, (B) Re = 163, (C) Re = 217, (D) Re = 186.6, (E) Re = 197 and (F) Re = 213, according to [56].

to save the droplet's initial shape, i.e. it helps to resist against deformation or movement. Comparison of the droplets with different density ratios demonstrates that droplets with higher density ratios have deformed less even in accelerating zones. In addition, the centrifugal force on the droplet is increasing with time which means that the final position of the droplet cannot be identified. At very large density ratios, e.g. $\rho_h/\rho_l = 100$, the droplet behaves like a very heavy solid sphere causing a chaotic unsteady flow pattern at any time.

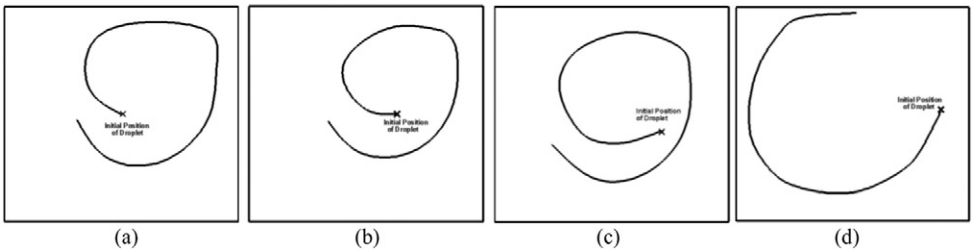

Fig. 29. Pathline of a droplet in a rotating flow with different initial positions: $\rho_h/\rho_l = 1$, data of the present study.

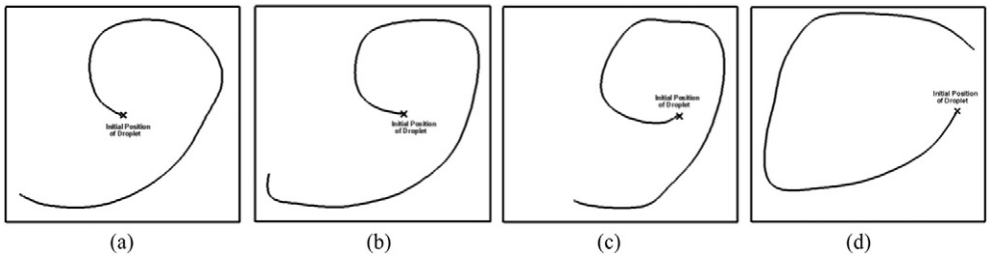

Fig. 30. Pathline of a droplet in a rotating flow with different initial positions: $\rho_h/\rho_l = 5$, data of the present study.

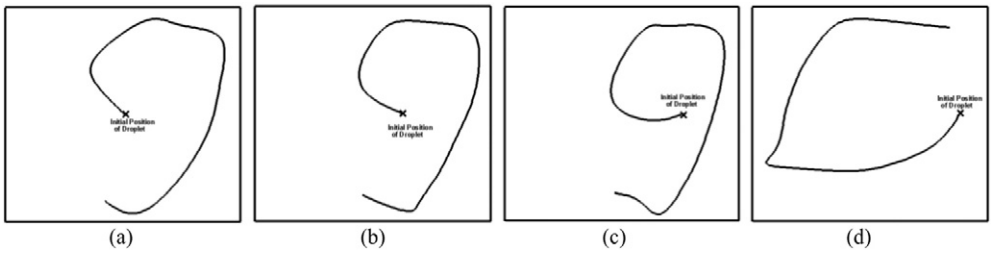

Fig. 31. Pathline of a droplet in a rotating flow with different initial positions: $\rho_h/\rho_l = 10$, data of the present study.

The analysis of the droplet trajectories for different initial positions proves that by increasing the density ratio, due to the higher inertia of the droplet and centrifugal forces, it would not go through the pathline of the main flow; the higher the density ratio, the larger the droplet trajectories deviate from the carrying flow pathline.

An important point that should be considered is that with increasing density ratios the droplet will get closer to the wall and it would be affected by the ground such that a lift force resulting from increasing pressure between the droplet and the wall will be exerted on the droplet and forces it to move away from the wall.

Also the droplet size has strong effects on its pathline. Increasing the droplet diameter leads to an increase in droplet mass or inertia. On the other hand, it decreases the absolute velocity of the droplet. The reduction of the absolute velocity exceeds the effects of the increased mass and decreased the centrifugal force. This fact causes the droplets with larger diameter to experience less centrifugal force and move in a pathline with a smaller radius.

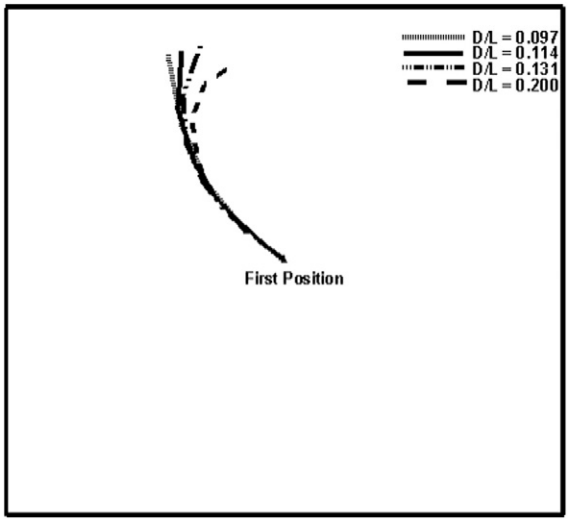

Fig. 32. Effect of diameter on pathlines of droplets, $\rho_h/\rho_l = 100$, data of the present study.

Acknowledgements

We would like to thank Abbas Fakhari for insightful discussions.

References

[1] Bruijin Rde, PhD Thesis, Eindhoven University of Technology, 1998.
[2] Taylor GI. Proc R Soc London, Ser A 1932;138:41–8.
[3] Taylor GI. Proc R Soc London, Ser A 1934;146:501–23.
[4] Chaffey CE, Brenner H. J Colloid Interface Sci 1967;24:258–69.
[5] Cox RG. J Fluid Mech 1969;37:601–23.
[6] Barthès-Biesel D, Acrivos A. J Fluid Mech 1973;61:1–21.
[7] Taylor GI. Proceedings of the 11th international congress of applied mechanics. 790-796 Munich: Springer; 1964.
[8] Buckmaster JD. J Fluid Mech 1972;55:385–400.
[9] Buckmaster JD. Trans ASME, Ser E, J Appl Mech 1973;40:18–24.
[10] Acrivos A, Lo TS. J Fluid Mech 1978;86:641–72.
[11] Rallison JM, Acrivos A. J Fluid Mech 1978;89:191–200.
[12] Hinch EJ, Acrivos A. J Fluid Mech 1979;91:404–14.
[13] Hinch EJ, Acrivos A. J Fluid Mech 1980;98:305–28.
[14] Yu W, Bousmina M, Grmela M, Palierne JF, Zhou C. J Rheol 2002;46:1381–99.
[15] Dressler M, Edwards BJ. Rheol Acta 2004;43:257–82.
[16] Li J, Renardy Y, Renardy M. Phys Fluids 2000;12:269–82.
[17] Renardy Y, Cristini V, Li J. Int J Multiphase Flow 2002;28:1125–47.
[18] Renardy Y, Renardy M. J Comput Phys 2002;183:400–21.
[19] Loewenberg M, Hinch EJ. J Fluid Mech 1996;321:395–419.
[20] Loewenberg M, Hinch EJ. J Fluid Mech 1997;338:299–315.
[21] Yon S, Pozrikidis C. Comput Fluids 1998;27:879–902.
[22] Pozrikidis C. J Comput Phys 2001;169:250–301.
[23] Cunha FR, Loewenberg M. Mech Res Commun 2003;30:639–49.
[24] Feigl K, Kaufmann SFM, Fischer P, Windhab EJ. Chem Eng Sci 2003;58:2351–63.
[25] Janssen PJA, Anderson PD. J Comput Phys 2008;227:8807–19.
[26] Rumscheidt FD, Mason SG. J Colloid Sci 1961;16:238–61.
[27] Torza S, Cox RG, Mason SG. J Colloid Interface Sci 1972;38:395–411.
[28] Grace HP. Chem Eng Commun 1982;14:225–77.
[29] Bentley BJ, Leal LG. J Fluid Mech 1986;167:219–40.
[30] Bentley BJ, Leal LG. J Fluid Mech 1986;167:241–83.
[31] Stone HA, Bentley BJ, Leal LG. J Fluid Mech 1986;173:131–58.
[32] Guido S, Villone M. J Rheol 1998;42:395–415.
[33] Guido S, Greco F, Villone M. J Colloid Interface Sci 1999;219:298–306.
[34] Guido S, Minale M, Maffetone PL. J Rheol 2000;44:1385–99.
[35] Guido S, Greco F. Rheol Acta 2001;40:176–84.
[36] Birkhofer BH, Eischen JC, Megias-Alguacil D, Fischer P, Windhab EJ. Ind Eng Chem Res 2005;44:6999–7009.
[37] Megias-Alguacil D, Feigl K, Dressler M, Fischer P, Windhab EJ. J Non-Newtonian Fluid Mech 2005;126:153–61.
[38] Javadi A, Kragel J, Pandolfini P, Loglio G, Kovalchuk VI, Aksenenko EV, et al. Colloids Surf A Physicochem Eng Asp 2010;365:62–9.
[39] Javadi A, Kragel J, Makievski AV, Kovalchuk VI, Kovalchuk NM, Mucic N, et al. Colloids Surf A Physicochem Eng Asp 2012;407:159–68.
[40] Javadi A, Karbaschi M, Bastani D, Ferri JK, Kovalchuk VI, Kovalchuk NM, et al. Colloids Surf A Physicochem Eng Asp 2014;441:846–54.
[41] Inamuro T, Tomita R, Ogino F. Int J Mod Phys 2003;17:21–6.
[42] van der Sman RGM, van der Graaf S. Comput Phys Commun 2008;178:492–504.

[43] Farokhirad S, Lee T, Morris JF. Commun Comput Phys 2013;13:706–24.
[44] Xin J, Megaridis CM. Int J Heat Fluid Flow 1996;17:52–62.
[45] Egholm RD, Fischer P, Feigl K, Windhab EJ, Kipka R, Szabo P. Chem Eng Sci 2008;63:3526–36.
[46] Poon EKW, Quan S, Lou J, Giacobello M, Ooi ASH. J Fluid Mech 2011;684:227–50.
[47] Arkhipov VA, Tkachenko AS, Usanina AS. J Eng Phys Thermophys 2013;86:567–76.
[48] Campero RJ, Vigil RD. Phys Rev Lett 1997;79:3897–900.
[49] Campero RJ, Vigil RD. Ind Eng Chem Res 1999;38:1094–8.
[50] Ravelet F, Delfos R, Westerweel J, Springer, Berlin Heidelberg, 2007.
[51] Zhu X, Vigil RD. AIChE J 2001;47:1932–40.
[52] Sathe MJ, Deshmukh SS, Joshi JB, Koganti SB. Ind Eng Chem Res 2010;49:14–28.
[53] Joseph DD, Nguyen K, Beavers GS. J Fluid Mech 1984;141:319–45.
[54] Joseph DD, Singh P, Chen K, Kramer L. In: Busse FH, editor. Nonlinear evolution of Spatio-temporal structures in dissipative continuous systems; 1990.
[55] Renard Y, Joseph DD. J Fluid Mech 1985;150:381–94.
[56] Qiao J, Deng R, Wang CH. Int J Multiphase Flow 2014;67:132–9.
[57] Shan X, Chen H. Phys Rev E 1993;47:1815–9.
[58] Swift MR, Osborn WR, Yeomans JM. Phys Rev E 1996;54:5041–52.
[59] Taeibi Rahni M, Karbaschi M, Miller R, CRC Press, 2015.
[60] Lee T. Comput Math Appl 2009;58:987–94.
[61] Lee T, Liu LJ. Comput Phys 2010;229:8045–63.
[62] Chen S, Doolen GD. Annu Rev Fluid Mech 1998;30:329–64.
[63] Succi S, Oxford University Press, Oxford.
[64] Hou S, Zou Q, Chen S, Doolen G, Cogley AC. J Comput Phys 1995;118:329–47.
[65] Sheth KS, Pozrikidis C. Comput Fluids 1995;24:101–19.
[66] Ghia U, Ghia KN, Shin CT. J Comput Phys 1982;48:387–411.
[67] Maneshian B, Javadi K, Taeibi Rahni M. Int J Flow Control 2015 [Accepted].